A&A 386, 1074–1102 (2002)
DOI: 10.1051/0004-6361:20020362

Astronomy & Astrophysics

CO and H_2O vibrational emission toward Orion Peak 1 and Peak 2

E. González-Alfonso[1,2], C. M. Wright[3,4], J. Cernicharo[1], D. Rosenthal[5], A. M. S. Boonman[3], and E. F. van Dishoeck[3]

[1] CSIC, IEM, Dpto. Física Molecular, Serrano 123, 28006 Madrid, Spain
[2] Universidad de Alcalá de Henares, Departamento de Física, Campus Universitario, 28871 Alcalá de Henares, Madrid, Spain
[3] Leiden Observatory, PO Box 9513, 2300 RA Leiden, The Netherlands
[4] School of Physics, University College, Australian Defence Force Academy, University of New South Wales, Canberra ACT 2600, Australia
[5] Max-Planck-Institut für Extraterrestrische Physik, Giessenbachstrasse, 85741 Garching, Germany

Received 4 December 2001 / Accepted 4 March 2002

Abstract. ISO/SWS observations of Orion Peak 1 and Peak 2 show strong emission in the ro-vibrational lines of CO $v = 1-0$ at 4.45–4.95 μm and of H_2O $\nu_2 = 1-0$ at 6.3–7.0 μm. Toward Peak 1 the total flux in both bands is, assuming isotropic emission, ≈2.4 and ≈0.53 $L_\odot$, respectively. This corresponds to ≈14 and ≈3% of the total H_2 luminosity in the same beam. Two temperature components are found to contribute to the CO emission from Peak 1/2: a warm component, with $T_k = 200$–400 K, and a hot component with $T_k \sim 3 \times 10^3$ K. At Peak 2 the CO flux from the warm component is similar to that observed at Peak 1, but the hot component is a factor of ≈2 weaker. The H_2O band is ≈25% stronger toward Peak 2, and seems to arise only in the warm component. The P-branch emission of both bands from the warm component is significantly stronger than the R-branch, indicating that the line emission is optically thick. Neither thermal collisions with H_2 nor with H I seem capable of explaining the strong emission from the warm component. Although the emission arises in the postshock gas, radiation from the most prominent mid-infrared sources in Orion BN/KL is most likely pumping the excited vibrational states of CO and H_2O. CO column densities along the line of sight of $N(\mathrm{CO}) = 5$–10×10^{18} cm^{-2} are required to explain the band shape, the flux, and the P-R-asymmetry, and beam-filling is invoked to reconcile this high N(CO) with the upper limit inferred from the H_2 emission. CO is more abundant than H_2O by a factor of at least 2. The density of the warm component is estimated from the H_2O emission to be $\sim 2 \times 10^7$ cm^{-3}. The CO emission from the hot component is neither satisfactorily explained in terms of non-thermal (streaming) collisions, nor by resonant scattering. Vibrational excitation through collisions with H_2 for densities of $\sim 3 \times 10^8$ cm^{-3} or, alternatively, with atomic hydrogen, with a density of at least 10^7 cm^{-3}, are invoked to explain simultaneously the emission from the hot component and that from the high excitation H_2 lines in the same beam. A jump shock is most probably responsible for this emission. The emission from the warm component could in principle be explained in terms of a C-shock. The underabundance of H_2O relative to CO could be the consequence of H_2O photodissociation, but may also indicate some contribution from a jump shock to the CO warm emission.

Key words. shock waves – ISM: abundances – ISM: individual objects: Orion

1. Introduction

The Orion molecular cloud embeds a complex molecular outflow with two main kinematic components associated with the corresponding spectral features and morphology: the low-velocity plateau, which extends in the northeast-southwest direction, and the high-velocity plateau, approximately perpendicular to this. The high-velocity plateau is associated with a bipolar outflow that contains the two brightest H_2 emission peaks in the sky: Peak 1 and Peak 2 (Beckwith et al. 1978).

Both peaks have been observed in the H_2 lines for more than 25 years with increasing angular and/or spectral resolution. Observations of other abundant species, namely CO and H_2O, which could test our understanding of the physics involved in those molecular shocks, are more scarce. Observations of pure rotational $v = 0$ CO lines in the millimetric (e.g., Rodríguez-Franco et al. 1999) are not sensitive to the temperature and density. In the far infrared, CO observations have lacked high angular

Send offprint requests to: E. González-Alfonso, e-mail: gonzalez@isis.iem.csic.es

resolution (e.g., Storey et al. 1981; Watson et al. 1985), so that the inferred physical conditions are an average over the entire Orion outflow, and mainly trace the low-velocity plateau. Detection of mid-infrared ro-vibrational CO lines by Geballe & Garden (1987, 1990; hereafter GG) had much better angular resolution, but were limited to a few lines from which the postshock gas conditions are difficult to retrieve. On the other hand, H_2O observations have been restricted for a long time to maser emission (e.g., Genzel et al. 1981; Cernicharo et al. 1994, 1999). Recent SWAS observations of the 557 GHz H_2O line trace the quiescent molecular cloud (Snell et al. 2000), and both the low-velocity and high-velocity flows (Melnick et al. 2000), but the H_2O emission in the high-velocity plateau is difficult to isolate.

The launch of ISO has opened the possibility of studying the Orion outflows in more detail. LWS observations of pure rotational CO (Sempere et al. 2000) and H_2O lines in emission (Cernicharo et al. 1999; Harwit et al. 1998) still lack angular resolution and mainly trace the low-velocity plateau. H_2O pure rotational lines seen in absorption in the SWS spectrum toward IRc2 (Wright et al. 2000) also trace the low-velocity flow. Nevertheless, SWS observations of the whole CO $v = 1{-}0$ at 4.7 μm and H_2O $\nu_2 = 1{-}0$ at 6.5 μm bands are very useful to study the molecular emission from Peak 1 and 2. Although with limited spectral resolution, the SWS angular resolution in the mid-infrared allows the high-velocity flow to be isolated from the low-velocity one. Very interestingly, the ISO/SWS beam for the CO and H_2O bands is the same as the beam for most of the H_2 lines studied by Rosenthal et al. (2000, hereafter RBD) in Peak 1, so that a direct comparison of the vibrational emission of the major coolants in the shock around this position can be performed. In this paper we study the CO and H_2O ro-vibrational bands as observed with ISO/SWS toward Peak 1 and Peak 2. We also present the ISO/SWS spectrum of CO toward IRc2. Absorption/emission in the H_2O ro-vibrational band toward IRc2 and BN has been studied by van Dishoeck et al. (1998) and González-Alfonso et al. (1998).

This paper is organized as follows. In Sect. 2 the data acquisition and reduction are described. The spectra and the relevant observational parameters are presented in Sect. 3. The analysis of the observations is developed in Sect. 4, where the physical processes and parameters involved in the observed emission are derived. In Sect. 5 we discuss the main results, and Sect. 6 summarizes our main conclusions.

2. Observations and data reduction

2.1. Observations

The full 2.4–45.2 μm spectrum of Orion Peak 1, obtained in the SWS01 observing mode (de Graauw et al. 1996) on UTC October 3 1997 (TDT = 68 701 515), was presented by RBD. We present a new reduction here. A higher spectral resolution spectrum of Peak 1, from 4.45 to 5.01 μm, was taken in the grating mode SWS06 in parallel to a Fabry-Perot SWS07 observation on October 3 1997 (TDT = 68 701 611). The Orion Peak 2 spectrum was obtained in the SWS01 observing mode only, TDT = 83301701, on February 25 1998. The central wavelengths of the CO $v = 1{-}0$ and H_2O $\nu_2 = 1{-}0$ bands are at 4.7 and 6.5 μm. The SWS06 observations have about the nominal SWS spectral resolution, which is 1500–1800–2500 and 1100–1300–1500 at 4.7 and 6.5 μm, respectively. The range of values corresponds to the full SWS resolving power of an extended source, a 15″ diameter source and a point source, respectively, as given by Lutz et al. (2000). Both SWS01 observations were taken with the slowest scan speed 4, yielding a resolving power that is a factor ∼1.4 lower than the nominal one (Leech et al. 2001). This results in SWS01 resolving powers of 1070–1280–1790 at 4.7 μm and 790–930–1070 at 6.5 μm, for the source extensions quoted above. The aperture size is $14'' \times 20''$ for both the CO and H_2O bands. It was centered at $\alpha(2000) = 05^h35^m13.7^s$, $\delta(2000) = -05°22'08.5''$ for Peak 1, and at $\alpha(2000) = 05^h35^m15.8^s$, $\delta(2000) = -05°22'40.7''$ for Peak 2. The long axis was oriented ∼5.5° E of N for both Peak 1 observations, and 169.5° for the Peak 2 observation.

2.2. Data reduction

Data were reduced using version 9.5 of the Off Line Processing (OLP) pipeline system. The Standard Processed Data (SPD) were examined for sudden signal jumps, which may indicate a pointing jitter, and consistency between the up and down scan directions. No problems were found. Further, as SWS band 2 may be subject to detector memory effects, we performed a special dark current subtraction within the Interactive Analysis (IA) software before deriving the Auto Analysis Result (AAR). When compared with the pipeline AAR the two reduction schemes agree well in terms of band shape, but the IA reduction resulted in a 10% lower flux. We here use fluxes derived from the pipeline reduction, which uses the most up-to-date relative spectral response and flux calibration files. Following the AAR stage, further data processing, such as flatfielding, sigma clipping and rebinning, was performed using software in either the IA or Observer's SWS IA (OSIA) version 2.0 software packages. Flatfielding was performed using a reference spectrum equal to a first order polynomial fit to the average of all down scan data for the CO and H_2O bands. This was followed by clipping any points more than 3 sigma outside of the average of all data within a bin equal to the theoretical resolving power, and subsequent rebinning using a bin equal to twice the spectral resolution.

3. Results

3.1. The CO v = 1–0 band

3.1.1. Peak 1 and Peak 2

Figure 1 shows the observed ISO/SWS06 and SWS01 spectra toward Peak 1, the SWS01 spectrum toward Peak 2, and the SWS06 spectrum toward IRc2, between 4.45 and 5 μm. Toward Peak 1/2, the continuum is nearly flat over that wavelength range, with a flux of 16–18 Jy at Peak 1 ($\approx 2.3\times10^{-16}$ W cm^{-2} μm^{-1}), and 10–12 Jy at Peak 2. The individual ro-vibrational lines of the CO $v=1-0$ band are clearly detected above the continuum with a typical flux of $\sim$9 Jy in the SWS01 spectrum. The corresponding flux is $\sim 5\times10^{-19}$ W cm^{-2}, only $\approx$8 and $\approx$4.5 times weaker than the 4.7 μm H_2 0–0 S(9) line at Peak 1 and Peak 2, respectively. In Fig. 1, we indicate the positions of some ^{13}CO $v=1-0$ and ^{12}CO $v=2-1$ lines that are not coincident with any ^{12}CO $v=1-0$ line. In the SWS06 spectrum of Peak 1, some weak features match the positions of ^{12}CO $v=2-1$ lines, but the match is not systematic. On the other hand, the ^{13}CO lines could be responsible for an apparent modulation of the continuum in the SWS01 data (see Sect. 4.4 and Fig. 16).

Figure 1 shows that the CO band toward Peak 2, although slightly weaker, displays a shape quite similar to that of Peak 1. Apart from the relative enhancement of the $P(1)$ and $P(2)$ lines toward Peak 2, the flux distributions observed toward both positions are nearly the same, and the $P(1)$ line may be contaminated by HI and [Fe II]. The similarity between the CO line fluxes at both positions is also striking because the H_2 0–0 S(9) line in Fig. 1 is stronger at Peak 1 by a factor of $\approx$1.8, which is in good agreement with the flux ratio obtained for the same H_2 line by GG. It is also worth noting in Fig. 1 that, at both positions, the $R-$branch is significantly weaker than the $P-$branch. Neither the uncertainties in the variation of the continuum flux across the band, nor the possible contamination of the $P-$branch by ^{13}CO lines, can account for this P-R-asymmetry. Our interpretation of this effect is given in Sect. 4.4.

Most of the CO lines observed in the SWS01 are consistent with a spectral resolution in the range 1050–1200, indicating that the emission is extended compared with the ISO/SWS beam. In the SWS06 spectrum of Peak 1 the line widths are 170–210 km s^{-1} ($\lambda/\Delta\lambda\sim1600$), also suggesting spatially extended emission. This is supported by the observations of GG, who found that the $P(8)$ line emission from the surroundings of Peak 1 (i.e., within the ISO/SWS beam) is extended, although far from uniform. On the other hand, adjacent $R-$lines are separated in velocity by more than 300 km s^{-1}, so that the individual lines do not blend in the SWS06 spectrum of Peak 1. Therefore, the continuum level can be correctly determined without line contamination. In the SWS01 spectrum, however, the lines blend partially in the $R-$branch and the continuum level becomes uncertain.

Figure 2a shows the spectra between 5 and 5.23 μm of Peak 1, Peak 2, and IRc2. Interestingly, the spectrum of Peak 1 shows a series of emission features that coincide rather well with the expected wavelengths of high-$P(J)$ CO lines, up to $J=48$. Although the RSRF (Relative Spectral Response Function) of band 2A shows, at these wavelengths, a faint hint of fringes, neither the expected height ($\leq$0.5 Jy versus typical observed intensities of 2.5–3 Jy) nor the fringe frequency agree with those of the observed features. The IRc2 spectrum (Fig. 2a), with a much stronger continuum, shows features with height and frequency similar to the fringes of the scaled RSRF, thus indicating that the RSRF estimate of fringes is accurate. Furthermore, inspection of the SPD data have shown that the "up" and "down" scans agree quite well, and both display these emission features. No signal jumps at the SPD level have been found. Therefore, we conclude that these features are not instrumental artifacts, i.e. fringes, but real CO lines, with typical fluxes of $\approx1.5\times10^{-19}$ W cm^{-2} at Peak 1 and weak J-dependence, indicative of the presence of a high temperature component. High $R(J)$ lines are also detected for $J>30$ (Fig. 2b), but the corresponding intensities are very uncertain due to partial blending. Peak 2 also shows high-J lines in the $P-$branch, but they are a factor $\sim$2 weaker than in the Peak 1 spectrum.

Line fluxes have been determined by fitting Gaussian curves to the spectral features. We estimate a line flux uncertainty arising from the spectral noise alone of 0.5×10^{-19} and 0.3×10^{-19} W cm^{-2} in the SWS06 and SWS01 spectra, respectively. However, the actual uncertainty in some wavelength ranges is significantly higher because of fluctuations and uncertainties in the continuum, blending with lines from other species, and partial blending with other CO lines in the R-branch. Figure 3 displays the fluxes toward Peak 1 and 2. The $P(J)$ and $R(J)$ line flux distributions show marked differences. In Fig. 3c we plot the normalized values of $F^T_{J_1}\equiv F^P_{J_1}+F^R_{J_1}$ against J_1, where J_1 is the rotational quantum number of the upper $v=1$ level, $F^P_{J_1}$ denotes the flux of the $P(J_1+1)$, and $F^R_{J_1}$ denotes that of the $R(J_1-1)$ line. From the shape of these distributions, it seems evident that at least two temperature components are necessary to account for the CO $v=1-0$ emission from both peaks. A hot component will be responsible for the emission from $J_1>25$, whereas a region with much more moderate temperature (a warm component) will account for the bulk of the emission from $J_1<25$ (Fig. 3c). The P-R-asymmetry is only related to this warm component, i.e., the fluxes of the $P(J_1+1)$ and $R(J_1-1)$ lines are similar for $J_1\geq23$ (Fig. 3).

A usual way to visualize the distribution of fluxes is the Boltzmann diagram of Fig. 4a, in which the upper level column densities have been calculated by assuming that the lines are optically thin, i.e.,

$$N_{\rm thin}(v=1,J)=\frac{4\pi10^7}{h\Omega_B}\times\frac{F^T_J({\rm W\,cm^{-2}})}{\nu^P_J A^P_J+\nu^R_J A^R_J}, \quad (1)$$

where A^P_J (A^R_J) is the Einstein coefficient for spontaneous emission of the $P(J+1)$ [$R(J-1)$] ro-vibrational line,

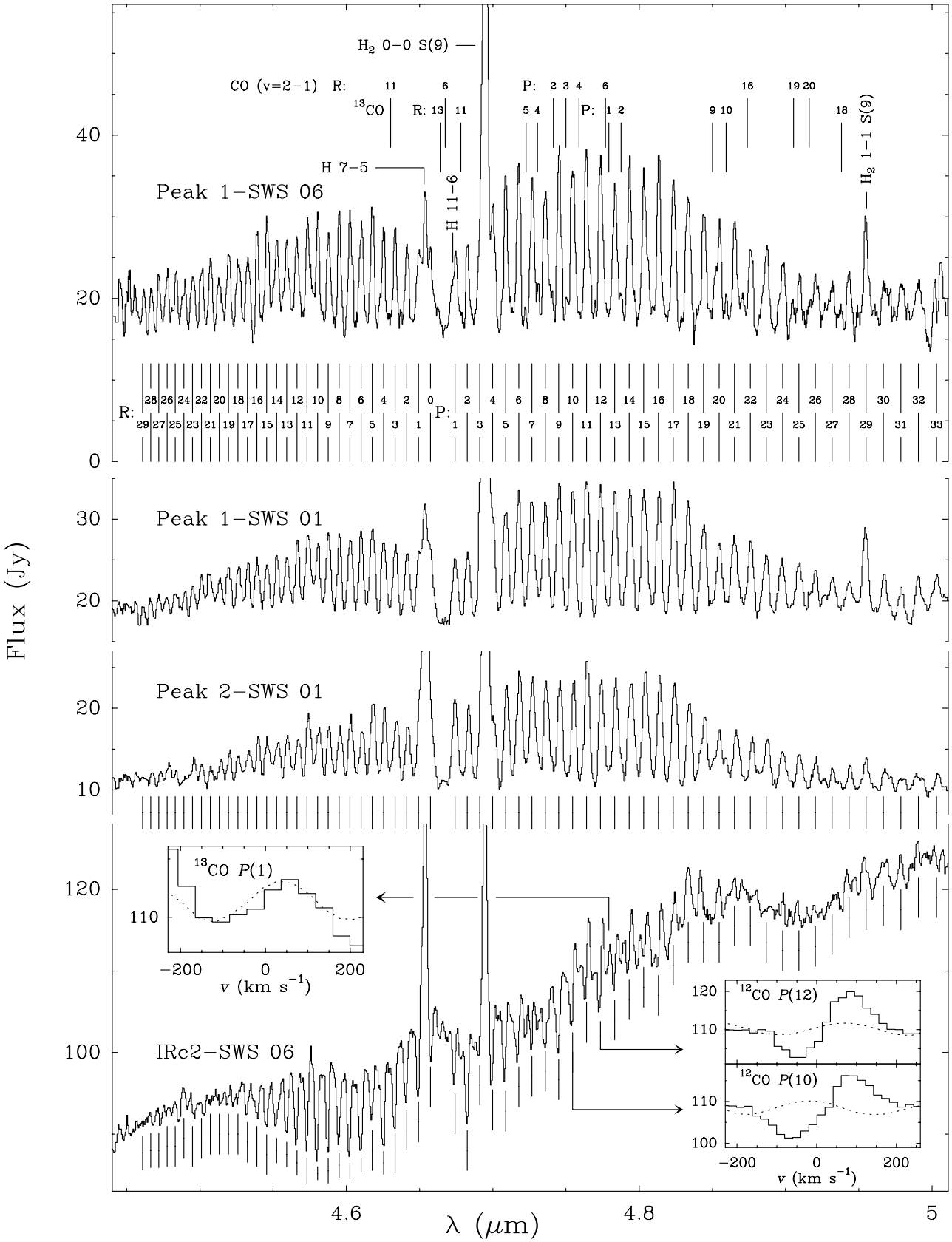

Fig. 1. Observed CO $v = 1{-}0$ band toward Orion/Peak 1 (SWS06 and 01 modes), Peak 2 (SWS01) and IRc2 (SWS06). In addition to the expected positions of the ^{12}CO $v = 1{-}0$ $P(J)$ and $R(J)$ lines, H_2 and HI lines, the positions of some ^{12}CO $v = 2{-}1$ and ^{13}CO $v = 1{-}0$ lines that are not coincident with any CO $v = 1{-}0$ line are also indicated in the upper spectrum. Insert panels show in more detail some profiles observed toward IRc2, and dashed lines indicate the RSRF scaled to the IRc2 continuum. The apparent ^{13}CO $P(1)$ line is an effect of fringes.

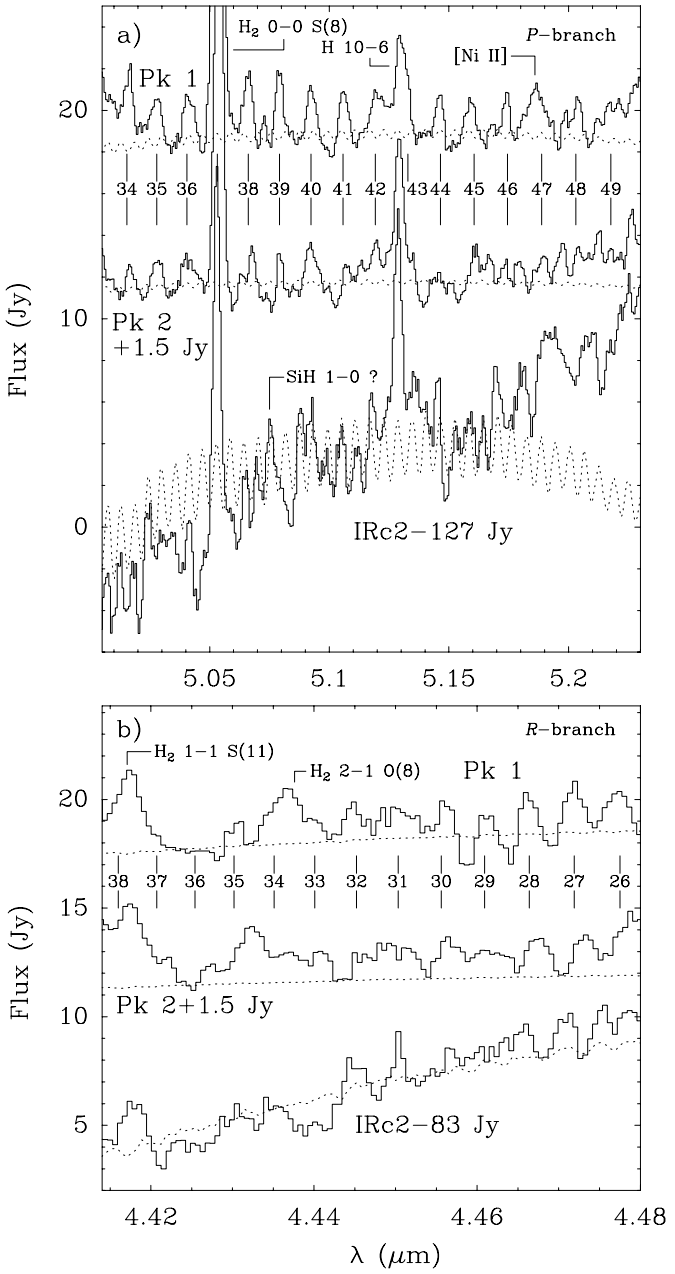

Fig. 2. Spectra around 5.12 and 4.45 μm observed towards Orion/Peak 1, Peak 2, and IRc2. The expected positions of the high-J CO $v = 1{-}0$ lines are labelled. Dashed lines indicate the expected RSRF scaled to the observed continuum.

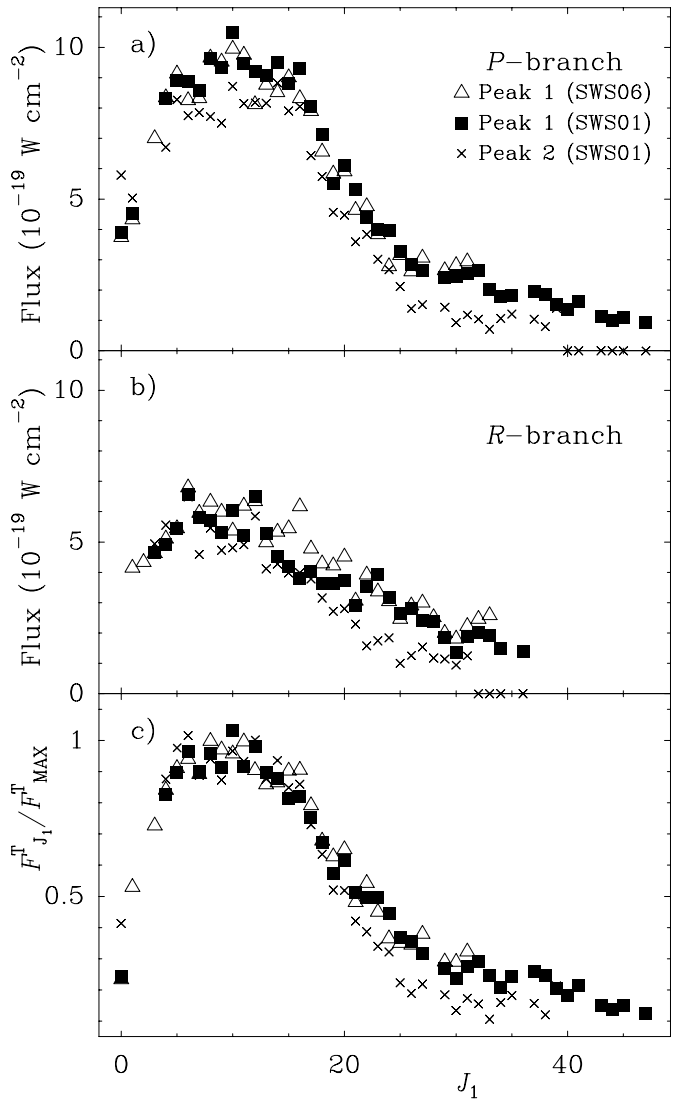

Fig. 3. CO $v = 1{-}0$ fluxes toward Peak 1 and Peak 2 in the **a)** $P-$ and **b)** $R-$branches, determined from Peak 1/SWS06 data (triangles), Peak 1/SWS01 data (squares), and Peak 2/SWS01 data (crosses), plotted against the rotational quantum number J_1 of the upper $v = 1$ level. **c)** Normalized values of $F^T_{J_1} \equiv F^P_{J_1} + F^R_{J_1}$. We have adopted maximum fluxes of $F^T_{\rm MAX} = 1.6 \times 10^{-18}$ W cm^{-2} for both SWS06 data (triangles) and SWS01 data (squares) of Peak 1, and $F^T_{\rm MAX} = 1.4 \times 10^{-18}$ W cm^{-2} for the Peak 2/SWS01 data. For $J_1 \geq 35$ (Peak 1) or $J_1 \geq 32$ (Peak 2), $F^R_{J_1}$ is calculated from $F^P_{J_1}$ by correcting for the Einstein-A coefficient and frequency.

ν analogously denotes the line frequencies, and Ω_B is the solid angle of the ISO/SWS beam. The distributions of Fig. 4a have been fitted to a two-temperature component (dashed lines). Although, as argued in Sect. 4.4, the CO emission from the warm component is optically thick, and in fact the fit for the low-J lines is not satisfactory, Fig. 4a gives a first rough estimate of the rotational temperatures of the warm and hot components: 400 K and 3×10^3 K, respectively. On the other hand, Fig. 4b shows that, apart from the few lowest-J lines, the lines with upper level energy up to 4×10^3 K (that include the contribution from both the warm and hot components) are ∼20% stronger at Peak 1, whereas the lines from the hot component are a factor ∼2 stronger toward that position.

In order to estimate the total emission in the band, we have adopted for Peak 1 fluxes of 6×10^{-19} and 2.5×10^{-19} W cm^{-2} for the $P(3)$ and $P(29)$ lines, respectively, and for Peak 2 fluxes of 5.5×10^{-19}, 6.2×10^{-19}, 1.3×10^{-19}, 4.1×10^{-19}, and 4.5×10^{-19} W cm^{-2} for the $P(3)$, $P(4)$, $P(29)$, $R(0)$, and $R(1)$ lines, respectively. These lines are blended with H_2 or H I lines, and our flux estimates are simple guesses based on the fluxes of

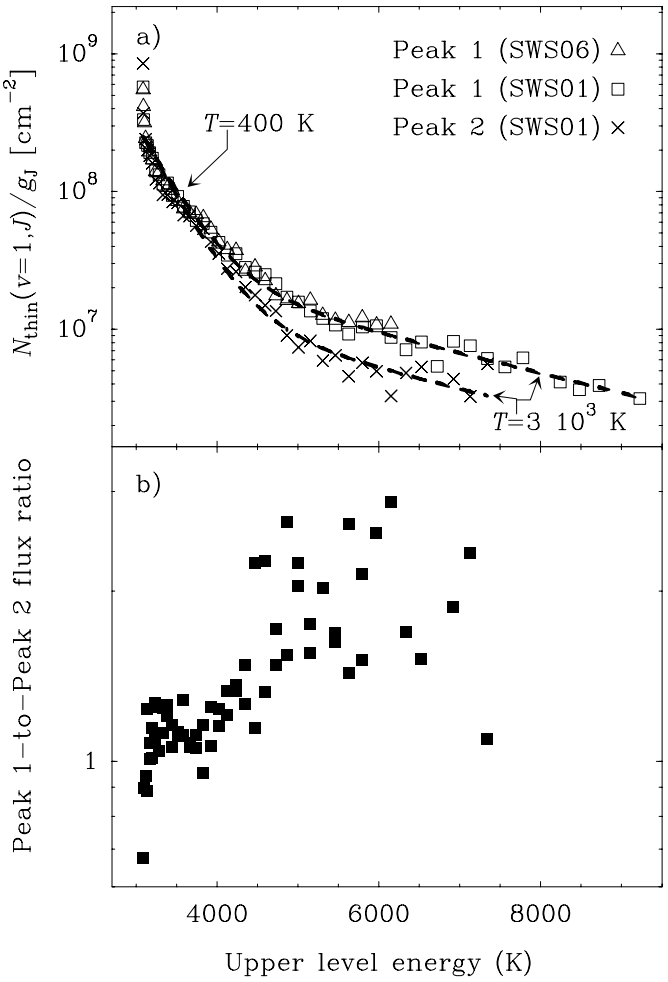

Fig. 4. a) Column densities of the CO $v = 1$ levels divided by the level degeneracy ($g_J = 2J + 1$), plotted against the upper level energy. Column densities are computed in the optically thin limit. **b)** Peak 1 to Peak 2 line flux ratios.

the adjacent J–lines. The fluxes of the $R-$branch lines with $J_1 \geq 35$ (for Peak 1) or $J_1 \geq 32$ (for Peak 2) have been determined from the corresponding $P-$branch lines by correcting for the Einstein-A coefficient and frequency. The resulting flux of the CO $v = 1-0$ band toward Peak 1 is 3.8×10^{-17} W cm^{-2} ($L \approx 2.4\ L_\odot$). The contribution of the hot component, assuming a Boltzman distribution at 3×10^3 K, is $\approx 1.7 \times 10^{-17}$ W cm^{-2}, so that the flux associated with the warm component is $\approx 2.1 \times 10^{-17}$ W cm^{-2}. Similarly, toward Peak 2 the total flux is $\approx 3.0 \times 10^{-17}$ W cm^{-2} (1.9 $L_\odot$), and the contributions of the warm and hot components are $\approx 2.1 \times 10^{-17}$ and $\approx 0.9 \times 10^{-17}$ W cm^{-2}, respectively. According to the extinction curve of RBD in Peak 1, and assuming similar extinction toward Peak 2, these fluxes could be ≈20% larger. The $P-$branch emission from the warm component (i.e., after subtraction of the emission from the hot one) is a factor of ≈2 stronger than the $R-$branch emission at both peaks.

Toward Peak 1, the $P(8)$ line has a flux of $\approx 1.3 \times 10^{-10}$ W cm^{-2} sr^{-1}, a factor of 1.5 lower than that measured by Geballe & Garden (1987) in a 5″ beam. On the other hand, the continuum intensity of $\approx 3.5 \times 10^{-8}$ W cm^{-2} μm^{-1} sr^{-1} is a factor of 1.4 larger than that measured by Grasdalen et al. (1992) with the KAO 15″ beam. Since there is observational evidence of marked spatial gradients in the emission of the CO $P(8)$ line (GG) and of the continuum (RBD) around Peak 1, we conclude that the fluxes measured by ISO are compatible with those previous determinations. In particular, the long axis of the ISO/SWS beam lies in the direction of the strong BN source (see RBD), and the continuum emission is expected to rise in this direction due to both scattering of radiation from BN by dust and/or thermal dust emission. Nevertheless, the ISO/SWS beam does not include BN itself, and the observed CO $v = 1-0$ emission must originate in the shock, rather than in the neighbourhood of BN. Scoville et al. (1983) found in the CO $v = 1-0$ spectrum toward BN an emission feature at 20 km s^{-1} with characteristic temperature of ∼600 K, but neither the line width nor the intensity are comparable with those of the $P(8)$ line observed toward Peak 1 (Geballe & Garden 1987).

3.1.2. IRc2

Toward IRc2 the CO band looks very different (Fig. 1). Most of the ^{12}CO $P-$branch lines show both emission and absorption ("P-Cygni" type profiles), despite the limited spectral resolution (>125 km s^{-1}). The deep absorption and strong emission of these lines cannot be ascribed to fringes (right-hand insert panels in Fig. 1). The spectrum also shows some apparent P-Cygni profiles that coincide in wavelength with the expected positions of ^{13}CO lines, but these features are an effect of fringes as the comparison with the RSRF scaled to the IRc2 continuum indicates (see the example in the left-hand insert panel of Fig. 1). The ^{12}CO $P(J \geq 17)$ lines, when detected, are in emission with little or no absorption. The $R-$branch lines tend to show also P-Cygni profiles, but the emission features in the $R-$branch are less prominent than those of the $P-$branch. The CO band shape toward BN (not shown) is also quite similar, and the CO line absorptions relative to the continuum are nearly the same.

These profiles qualitatively resemble those of some H_2O pure rotational lines around 40 μm observed with Fabry-Perot (Wright et al. 2000). In the case of CO, however, the absorption is expected to be much more spatially restricted to the direction of IRc2, because the emission at mid-infrared wavelengths peaks much more sharply around IRc2 than the extended far infrared emission (Wynn-Williams et al. 1984; Gezari et al. 1998). Evans et al. (1991) observed some ^{13}CO $P(J = 9$–$17)$ and ^{12}CO $P(J = 22$–$27)$ lines in the direction of IRc2 with a 3″–4″ beam and ≈25 km s^{-1} spectral resolution, finding P-Cygni profiles as in the present case. In both cases, and according with the line velocity coverage, the emission/absorption was ascribed to the low-velocity plateau. In particular, Evans et al. (1991) showed that the velocities of the absorption and emission peaks of the CO

lines differ by about 30 $\mathrm{km\,s^{-1}}$. In the present case it is however unclear, given our poor spectral resolution and the consequent fill in of the absorption by the emission, if the low-velocity flow alone can account for the observed profiles and strengths; in principle, some contribution of the high-velocity flow cannot be disregarded. In fact the $P(22)$ line detected by Evans et al. (1991) has emission and absorption features with similar strengths separated $\approx$27 $\mathrm{km\,s^{-1}}$, and in the ISO/SWS spectrum this line is hardly detected, because of the close cancellation between both components (Fig. 1). Nevertheless, lower-J lines in the low-velocity flow have much larger opacities than the $P(22)$ and could contribute to or even match the observed pattern.

Either way, the absorption features of the lowest-J lines are stronger than the emission features, probably due to the absorption by the foreground quiescent cloud. The P-Cygni profiles are a strong indication of radiative pumping of the CO $v = 1$ state, and the difference in intensity between the emission components of the $P-$ and $R-$branches resembles the behaviour of the H_2O $\nu_2 = 1{-}0$ band toward BN (González-Alfonso et al. 1998), for which the $P-$branch was observed in emission and the $R-$branch in absorption. Similar radiative transfer effects are presumably causing the CO pattern observed toward IRc2, as well as the P-R-asymmetry in CO and H_2O observed toward Peak 1 and Peak 2 (Sect. 4.4).

3.2. The H_2O $\nu_2 = 1{-}0$ band

Figure 5a displays the observed 5.8–7.2 μm spectrum toward Peak 1 and Peak 2. Those toward IRc2 and BN have been presented by van Dishoeck et al. (1998) and González-Alfonso et al. (1998). Besides strong H_2 and [Ar II] lines, weaker atomic hydrogen lines, and PAH emission at 6.2 μm, the spectrum shows a forest of features that correspond to the H_2O $\nu_2 = 1{-}0$ ro-vibrational lines. After subtracting the continuum emission (broad dashed lines), Figs. 5b,c show the resulting spectra where the positions of the strongest and/or low-lying H_2O lines are indicated.

The determination of fluxes has been carried out by fitting Gaussian curves to the observed features coincident with the positions of H_2O lines. Most of the observed profiles are best matched with $\lambda/\Delta\lambda \approx 800$, which suggests – as in the case of CO – that the emission fills the ISO/SWS beam. The fits are shown in Figs. 5b,c with dashed lines. The assigned individual fluxes are in some cases doubtful because of the close blending of lines at some wavelengths (Fig. 5). Despite this, we show in Fig. 6a the corresponding Boltzmann diagram, where the upper level column densities are computed in the optically thin limit from

$$N_{\rm thin}(\nu_2 = 1, J_{K_+K_-}) = \frac{4\pi 10^7}{h\Omega_{\rm B}} \times \frac{\sum F(\nu_2 = 1-0, J_{K_+K_-} - J'_{K_+K_-})(\mathrm{W\,cm^{-2}})}{\sum(\nu A)(\nu_2 = 1-0, J_{K_+K_-} - J'_{K_+K_-})}, \quad (2)$$

where the summations extend to all the detected lines with $J_{K_+K_-}$ as the upper level of the transition, and F denotes the fluxes. The distribution of Fig. 6a can be fitted with a straight line giving a rough estimate of the rotational temperature in the H_2O $\nu_2 = 1$ state, $\approx$150 K. According to our analysis in Sect. 4.4.3, the ro-vibrational H_2O lines with upper level energy $E_{\rm u} > 2650$ K are optically thin, but most lines with $E_{\rm u} < 2600$ K are optically thick. As a consequence, the column densities for the latter lines are underestimated in Fig. 6a, and therefore the fitted temperature of 153 K may be considered an upper limit. This temperature is much lower than the energy of the H_2O $\nu_2 = 1$ state above the ground vibrational state. Unlike the CO emission, there is no evidence for H_2O emission from a hot component, so that we will assume that the H_2O emission arises entirely from the warm component detected in the low-J CO lines.

As in the case of the CO band, the H_2O $R-$branch is weaker than the $P-$branch at both peaks. Only three – weak – lines below 6.3 μm are detected (Fig. 5b): $\nu_2 = 1{-}0$ $3_{03}\rightarrow 2_{12}$ (merging with $2_{12}\rightarrow 1_{01}$), $2_{21}\rightarrow 1_{10}$, and $1_{10}\rightarrow 1_{01}$ (unfortunately, in Peak 1 this line lies in a region of fringes around the PAH feature). This asymmetry is further discussed in Sect. 4.4.

Figure 6b shows that most lines display similar fluxes toward both peaks, but there are a few lines stronger at Peak 2 by more than 50%. Some of these flux ratios are uncertain because the corresponding lines merge with others (i.e., the H_2O $\nu_2 = 1{-}0$ $3_{03}\rightarrow 3_{12}$, $2_{20}\rightarrow 3_{31}$, $2_{02}\rightarrow 3_{13}$, and $1_{10}\rightarrow 1_{01}$, as well as the $0_{00}\rightarrow 1_{11}$), but the rest indicate unambiguously striking differences in flux between both peaks (H_2O $\nu_2 = 1{-}0$ $3_{30}\rightarrow 4_{41}$, $3_{21}\rightarrow 4_{32}$, $4_{14}\rightarrow 5_{05}$, $3_{12}\rightarrow 4_{23}$; see Fig. 5c) and have relatively high upper level energies (>2500 K). However, not all of the observed H_2O lines are stronger toward Peak 2. In particular, the joint emission in the $R-$branch of the H_2O $\nu_2 = 1{-}0$ $2_{12}\rightarrow 1_{01}$ and $3_{03}\rightarrow 2_{12}$ lines is somewhat stronger toward Peak 1 (Fig. 5b).

The total band flux is more reliable than the individual line fluxes. We find values of 7.1×10^{-18} and 8.8×10^{-18} $\mathrm{W\,cm^{-2}}$ toward Peak 1 and 2, respectively. However, there will be an additional contribution from some H_2O lines merging with the strong H_2 line at 6.1 μm, and also from other lines with flux densities below the noise level of 1.5 Jy but giving all together a significant contribution to the total emission. This unobserved contribution has been estimated from the models discussed in Sect. 4.4.3 to be roughly 20% of the total observed flux, so that we adopt a total band flux of 8.5×10^{-18} and 10.6×10^{-18} $\mathrm{W\,cm^{-2}}$ (luminosities of 0.53 and 0.67 $L_\odot$) toward Peak 1 and 2, respectively. According to the extinction curve of RBD in Peak 1, and assuming a similar extinction toward Peak 2, these values could be $\approx$10% larger.

The H_2O band strength toward Peak 2 is then a factor of 1.25 larger than toward Peak 1, and as shown above, the CO band emission associated with the warm component is similar toward both peaks. As in the case of the CO band,

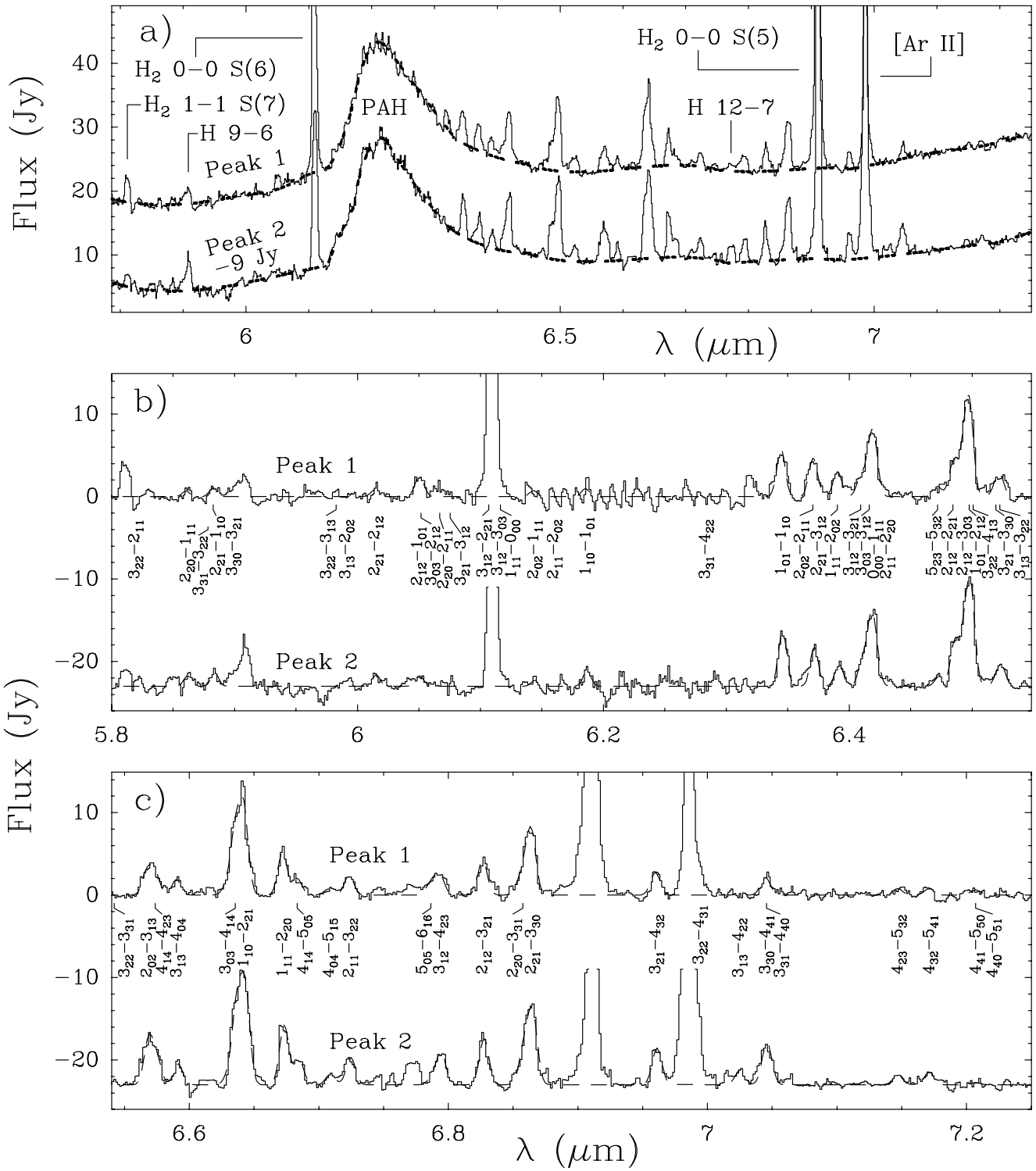

Fig. 5. a) Observed 5.8–7.2 μm spectrum toward Orion/Peak 1 and Peak 2. The dashed lines indicates the adopted continuum emission. Panels **b)** and **c)** show the resulting spectra after subtracting the above continuum. The positions of some H_2O $\nu_2 = 1{-}0$ ro-vibrational lines are indicated, and dashed lines show Gaussian fits to the spectral features coincident with H_2O lines.

the similarity of the H_2O bands toward both peaks indicates similar physical conditions in the opposite regions of the flow where the emission arises. Although the combined effect of different extinction and relative calibration could modify the relative fluxes to some extent, a significant spatial gradient of the H_2O $\nu_2 = 1{-}0$–to–H_2 and CO $v = 1{-}0$–to–H_2 flux ratios between both positions will still remain: the H_2 0–0 S(5) and S(6) lines in Fig. 5

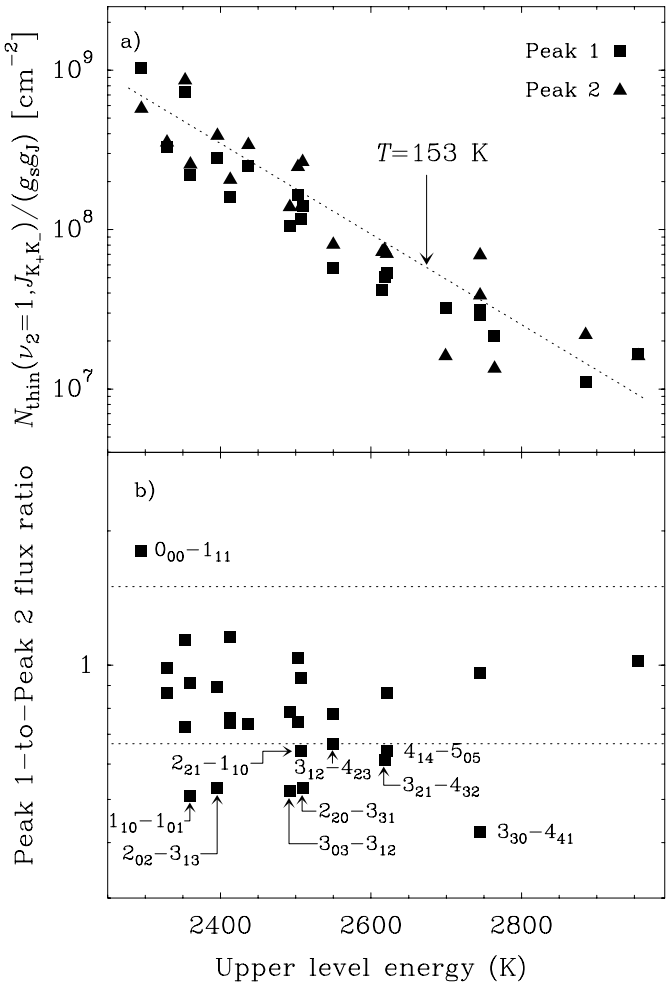

Fig. 6. a) Column densities of the H_2O $\nu_2=1$ levels (squares: Peak 1; triangles: Peak 2), divided by the level degeneracy ($g_s = 3$ for ortho-levels and 1 to para-levels; $g_J = 2J+1$), plotted against the upper level energy. Column densities are computed in the optically thin limit. **b)** Peak 1 to Peak 2 line flux ratios. Only those lines with fluxes larger than 6×10^{-20} W cm^{-2} toward both peaks are accounted for. Lines are labelled when fluxes at both peaks differ in more than 50%, i.e. when the corresponding flux ratio lies out from the region between the dotted lines.

and the 0–0 S(9) line in Fig. 1 are factors 1.5, 1.4 and 1.8 stronger toward Peak 1 than toward Peak 2, respectively. Whilst the H_2 lines are primarily sensitive to temperatures larger than ∼500 K, the Boltzmann diagrams of Figs. 4a (warm component) and 6a indicate more moderate temperatures.

3.3. Comparison between the observed luminosities and shock model predictions

The CO $v = 1$–0 and H_2O $\nu_2 = 1$–0 luminosities at Peak 1 are 2.4 $L_\odot$ and 0.53 $L_\odot$, i.e. 14% and 3% of the total H_2 luminosity in the same aperture (RBD), respectively. At this point, and prior to the data analysis, it is illustrative to compare the observed emission with predictions for shock models. These models, in which the CO and H_2O ro-vibrational emission are assumed to originate from *thermal collisions* in the postshock region, underestimate the fluxes we find in Orion Peak 1/2. For example, the $P(15)$ line flux in Peak 1 (1.4×10^{-10} W cm^{-2} sr^{-1}) is more than 20 times larger than in the Orion C-shock model of Draine & Roberge (1982). Draine & Roberge (1984) were able to predict CO $v = 1$–0 line fluxes in excess of 10^{-11} W cm^{-2} sr^{-1} for C-shock velocities larger than 35 km s^{-1}, but in these models the $R(20)$ line is significantly stronger than the $R(10)$ line, contrary to what is observed. In the C-shock model of Kaufman & Neufeld (1996a), the cooling by H_2O vibrational emission is predicted to be about one order of magnitude larger than that by CO. Also, both the rotational and the vibrational cooling by H_2 are expected to be more than 10^3 times that of vibrational CO for moderate preshock densities. At higher densities (Kaufman & Neufeld 1996b), the H_2 cooling is greatly reduced due to efficient collisional deexcitation, but the relative cooling of vibrational CO and H_2O still remains similar. Combinations of slow and fast C-shocks based on the models of Kaufman & Neufeld have accounted for the H_2 emission from Peak 1 (RBD) and Peak 2 (Wright 2000), but these will hardly account for the CO and H_2O band emission provided that the temperatures and densities involved in both shocks are not much larger than in the works of Draine & Roberge (1982, 1984) and that the covering factor of the high density component is low. On the other hand, J-type shocks (Hollenbach & McKee 1989, hereafter HM; Neufeld & Dalgarno 1989) neither can account for the H_2O band emission, since the temperature at which H_2O is formed is lower than the temperature profile across C-shocks. The excess of CO vibrational emission was first recognized by Geballe & Garden (1987), and one important goal of this paper is to shed light on the possible excitation mechanism of the CO $v = 1$ and H_2O $\nu_2 = 1$ states.

4. Analysis

It is usually accepted that, in molecular shocks, the molecular levels involved in observed emission lines are pumped by collisions with H_2. This is justified in view of the enhancement of temperature and density in the postshock gas. This is valid for most molecular transitions and in most sources, but the case may be different for some infrared molecular lines in regions where the radiation field in the infrared is enhanced because of the presence of newly-born high-mass stars. In the vicinity of the Kleinmann-Low Nebula the radiation field below 10 μm is strong and dominated by the BN and IRc2 stellar sources. Although Peak 1 is located at an angular distance of ≈15″ from BN (10^{17} cm at 450 pc), and Peak 2 is at ≈20″ from IRc2, the CO and H_2O ro-vibrational lines at 4.7 and 6.3 μm have large Einstein coefficients (∼15 s^{-1} for CO and ∼10 s^{-1} for the strongest H_2O transitions) and the possibility that the excited vibrational states are radiatively pumped must be evaluated.

4.1. Kinetic temperature

In order to discriminate between radiative and collisional excitation, the kinetic temperature (T_k) of the emitting gas must be estimated from the rotational distribution of the line fluxes. The CO $v = 1{-}0$ band is used for this analysis. However, the determination of T_k from the CO band shape is not obvious, because (*i*) T_k and the density are coupled parameters and the latter is not well constrained; (*ii*) there must be a gradient of physical conditions in the extended region that lies within the ISO/SWS beam, at least as a consequence of the cooling by the postshock gas; (*iii*) if the CO $v = 1$ state is pumped by radiation from BN, line opacity effects will alter the value derived for T_k; if it is pumped by collisions, uncertainties in T_k will also stem from the unknown state-to-state ro-vibrational collisional rates. This problem is, however, lessened because of the expected validity of the scaling relationships among the collisional rates that follow from the application of the infinite order sudden approximation (IOSA), as shown below. On the other hand, we start by assuming that the lines are optically thin, but relax this assumption later.

Statistical equilibrium applied to the populations of the $v = 1$ state of CO implies, in the optically thin limit,

$$n_{1,J_1} = \left[A^P_{J_1} + A^R_{J_1}\right]^{-1} \frac{\mathrm{d}n^+_{1,J_1}}{\mathrm{d}t}, \quad (3)$$

where n_{1,J_1} is the population of the ($v = 1$, J_1) level, and $\mathrm{d}n^+_{1,J_1}/\mathrm{d}t$ denotes the rate at which CO molecules are pumped from the $v = 0$ state to the ($v = 1$, J_1) level. Equation (3) implicitly assumes that a molecule pumped to a rotational level of $v = 1$ will leave it by always decaying to the ground v-state through spontaneous emission. This is very accurate because the probability of vibrational spontaneous de-excitation ($\approx$30 s^{-1}) is much larger than the probability for both spontaneous rotational de-excitation and vibrational/rotational relaxation through collisions for the densities and temperatures of interest (see below). The addition of the emissivities of the P- and R-lines that merge from a common ($v = 1$, J_1) level yields

$$\epsilon^T_{J_1} \equiv \epsilon^P_{J_1} + \epsilon^R_{J_1} = \frac{h\alpha}{4\pi} \times \frac{\mathrm{d}n^+_{1,J_1}}{\mathrm{d}t}, \quad (4)$$

where $\epsilon^P_{J_1}$ [$\epsilon^R_{J_1}$] is the emissivity of the $P(J_1{+}1)$ [$R(J_1{-}1)$] line, and

$$\alpha = \frac{\nu^P_{J_1} A^P_{J_1} + \nu^R_{J_1} A^R_{J_1}}{A^P_{J_1} + A^R_{J_1}} \quad (5)$$

is independent of J_1. Since $\epsilon^T_{J_1}$ is proportional to the sum of the fluxes of the corresponding P- and R- lines, $F^P_{J_1} + F^R_{J_1}$, T_k can be inferred from the comparison of the J_1-distribution of $\mathrm{d}n^+_{1,J_1}/\mathrm{d}t$ with that of the observed $F^P_{J_1} + F^R_{J_1}$ values shown in Fig. 3c.

4.1.1. Radiative pumping

Assuming that CO molecules scatter the radiation coming from a stellar source with effective radius r_s and temperature T_s, the pumping rate is given by

$$\frac{\mathrm{d}n^+_{1,J_1}}{\mathrm{d}t} = \frac{r_s^2}{4r^2} g_{J_1} 10^{-0.4\mathcal{A}_{4.7}} \left[\frac{A^R_{J_1}}{\exp\{h\nu^R_{J_1}/(kT_s)\} - 1} \frac{n_{0,J_1-1}}{g_{J_1-1}} + \frac{A^P_{J_1}}{\exp\{h\nu^P_{J_1}/(kT_s)\} - 1} \frac{n_{0,J_1+1}}{g_{J_1+1}} \right], \quad (6)$$

where $g_J = 2J + 1$, r is the distance between the star and the emitting CO molecules, and $\mathcal{A}_{4.7}$ is the extinction of the 4.7 μm stellar radiation along that path. Equation (6) neglects opacity effects in the CO ro-vibrational lines and, within this approximation, shows that the rotational distribution of $\epsilon^T_{J_1}$ will resemble that of the vibrational ground state populations. These $v = 0$ rotational levels are excited through collisions with H_2.

Figure 7 compares the predicted and observed distributions for various physical conditions. Following Lee & Draine (1985) we simulate the radiation field from BN by a blackbody of $T_s = 1100$ K, but results depend little on this choice. Figure 7a shows the results that assume an LTE distribution of populations in $v = 0$, which are appropriate if the CO $v = 0$ rotational levels are (nearly) thermalized. In this case, kinetic temperatures of 500 K ($\pm$50 K) and $\sim 3 \times 10^3$ K ($\pm$600 K) are derived for the warm and hot component, respectively. Non-LTE (NLTE) results are obtained by computing the rotational distribution of populations in the $v = 0$ state with the use of the Schinke et al. (1985) CO-$p$$H_2$ collisional rates. The dotted thin line in Fig. 7a displays the expected NLTE distribution for $n(H_2) = 10^7$ cm^{-3} and $T_k = 3 \times 10^3$ K. It remains close to the 3×10^3 K LTE one; however, lower densities would require higher T_k to match the distribution. In Fig. 7b (solid line) we adopt an H_2 density of $n(H_2) = 10^6$ cm^{-3} for the warm component. In the optically thin limit, and since the $v = 0$ rotational levels are not thermally populated, the warm component is fitted with $T_k = 650$ K, a value significantly larger than the LTE one. These optically thin models underestimate seriously the emission from low J_1, so that a better fit is achieved by including the scattering from a cold component (dashed thick line in Fig. 7a). Figures 7c and d show that the same physical conditions also match approximately the flux distribution for Peak 2, although the relative weights of the warm and hot components are different from those of Peak 1.

The above fits are based on single-T_k models for the warm and hot components, and therefore are far from being unique. An acceptable LTE fit to the warm component of Peak 1 (from $J_1 = 8$ to 24) is also obtained by including two T_k components with suitable weights (e.g., $T_k = 400$ and 600 K, or $T_k = 250$ and 550 K). Similarly, the flux distribution of the hot component ($J_1 > 25$) may be reproduced with two temperature components at $T_k = 2{\times}10^3$ K

and 3.6×10^3 K, where the former dominates the emission from the $J_1 < 38$ lines, or $T_{\rm k} = 1.6\times10^3$ K and 3.6×10^3 K, where the former dominates for $J_1 < 30$. The lack of spectral and angular resolution prevents the separation between the possible several $T_{\rm k}$ components, although we can conclude that components with $T_{\rm k} \leq 1200$ K will have negligible contribution to the observed emission from the hot component.

Opacity effects have been tested with the use of the radiative transfer code described in González-Alfonso & Cernicharo (1997), and are shown with dashed lines in Figs. 7b and d. The model consists of a spherical shell of radius 2.1×10^{17} cm ($\approx30''$ at 450 pc), which is illuminated by an isotropic radiation field represented by a blackbody at 1100 K diluted by the geometrical factor $\pi r_{\rm s}^2/r^2$. Only the emission from the spherical cocoon that subtends a solid angle equal to that of the ISO/SWS beam is considered (see Fig. 12 and Sect. 4.2.4). In our code the velocity field can be characterized by an expansion velocity ($v_{\rm e}$) and/or a microturbulent velocity ($v_{\rm t}$). In Figs. 7b and d, results for the "pure microturbulent" models are shown (i.e., $v_{\rm e} = 0$); these only depend on the $N({\rm CO})/v_{\rm t}$ ratio, where $N({\rm CO})$ is the radial column density of CO. The actual (beam-averaged) column density will be a factor $\approx$5.7 larger due to the contribution of the near and far sides of the shell and to the curvature of the spherical cocoon that lies within the beam (Fig. 12). If the opacities of the ro-vibrational lines become significant, the predicted band shape broadens: with the increase of $N({\rm CO})$, the flux of the most saturated lines ($J_1 = 6$–10) remains nearly constant, while the fluxes of the less thick lines continue increasing. The broadening of the flux distribution implies that lower $T_{\rm k}$ values must be invoked to match the band shape. The following conclusions are achieved: (*i*) for H_2 densities high enough to thermalize the $v = 0$ rotational levels ($n(H_2) = 5\times10^6$ cm^{-3}), $T_{\rm k} = 300$ K and $N({\rm CO})/v_{\rm t} = 6.6\times10^{16}$ cm^{-2}/(km s^{-1}) provide the best single-$T_{\rm k}$ fit to the data (dotted lines in Figs. 7b and d); (*ii*) If $n(H_2)$ is decreased by one order of magnitude, the data points are also matched with similar $N({\rm CO})/v_t$ but with $T_{\rm k} \approx 380$ K (dashed-dotted lines); (*iii*) the half-power linewidths (HPW) of the CO $P(8)$ line observed toward Peak 1/2 are of order 50–100 km s^{-1} (GG), and are matched with $v_{\rm t} = 15$–30 km s^{-1} (the CO $P(8)$ line is broadened due to opacity effects by a factor of $\sim$2 relative to the optically thin case); therefore, from these models we obtain a radial column density $N({\rm CO}) = 1$–2×10^{18} cm^{-2}; (*iv*) a lower limit for $T_{\rm k}$ is 200 K, for which $N({\rm CO})/v_{\rm t} = 2.6\times10^{17}$ cm^{-2}/(km s^{-1}) (short dashed lines); this model overestimates the flux of the low-J_1 lines and underestimates the flux of the $J_1 = 20$–24 lines; (*v*) a model composed of two spherical shells at 200 and 400 K, and $N({\rm CO})$ decreasing with larger $T_{\rm k}$, also yields a reasonable fit to the data (long-dashed lines). (*vi*) Models in which the lines are mainly broadened by a systematic velocity field (not shown) yield lower values for $T_{\rm k}$ ($\sim$250 K) and for $N({\rm CO})$ (by a factor of $\sim$2), and are further discussed in Sects. 4.2.4 and 4.4.2. In Sect. 4.4 arguments are given that support that the lines are optically thick.

4.1.2. Collisional pumping

For collisional pumping we have:

$$\frac{{\rm d}n^+_{1,J_1}}{{\rm d}t} = n_c \sum_{J_2} n_{0,J_2} k_{0,J_2\rightarrow1,J_1}(T_{\rm k}), \quad (7)$$

where $k_{0,J_2\rightarrow1,J_1}$ is the thermal-averaged rate for CO collisional excitation from the ($v = 0$, J_2) to the ($v = 1$, J_1) level (J_1 and J_2 denote rotational quantum numbers), and $n_{\rm c}$ is the number density of the collisional partner.

Apart from vibrational excitation of H_2, state-to-state collisional rates for ro-vibrational transitions are only available for the SiO-He system (Bieniek & Green 1983, hereafter BG). Nevertheless, the large number of degrees of freedom in Eq. (7) is greatly reduced provided that the IOSA can be applied (Parker & Pack 1978). The IOSA treats the rotational levels of the molecule as degenerate, and assumes that the relative angle between the collisional partners is held fixed during the collision; it is expected to be valid whenever the collisional kinetic energy is large compared to the rotational energy spacing. In such a case the cross sections and thermal averaged collisional rates for de-excitation from the ($v = 1$, J_1) molecular level to the ($v = 0$, J_2) one can be scaled from only one column of values:

$$k_{1,J_1\rightarrow0,J_2} = g_{J_2} \sum_{J_3=|J_1-J_2|}^{J_1+J_2} C^2(J_1J_2J_3;000) k_{1,J_3\rightarrow0,0}, \quad (8)$$

where $C(J_1J_2J_3;000)$ are the Clebsch-Gordan coefficients. DePristo et al. (1979) have shown that approximate corrections for the finite rotational spacing can be done by restricting the scaling relationships of Eq. (8) to downward transitions (as indicated), and calculating the upward transition rates from microscopic reversibility (although the $v = 0$, $J \geq 33$ levels of CO are above the $v = 1$, $J = 0$ one, Eq. (8) is valid provided that the $k_{1,J_3\rightarrow0,0}$ for $J_3 > 30$ are small enough). Insertion of Eq. (8) into Eq. (7) yields

$$\frac{{\rm d}n^+_{1,J_1}}{{\rm d}t} = g_{J_1} \exp\left\{-\frac{E_{1,J_1}}{kT_{\rm k}}\right\} \times \sigma(J_1), \quad (9)$$

where E_{1,J_1} is the energy of the ($v = 1$, J_1) level, and

$$\sigma(J_1) = n_{\rm c} \sum_{J_3} g_{J_3} k_{1,J_3\rightarrow0,0} \times \sum_{J_2} \frac{n_{0,J_2}}{g_{J_2}} \exp\left\{\frac{E_{0,J_2}}{kT_{\rm k}}\right\} C^2(J_1J_3J_2;000), \quad (10)$$

where J_2 runs from $|J_1 - J_3|$ to $J_1 + J_3$. Equations (4) and (9) show that the J_1-dependence of $\epsilon^T_{J_1}$ is the convolution of a Boltzmann distribution with that given by $\sigma(J_1)$

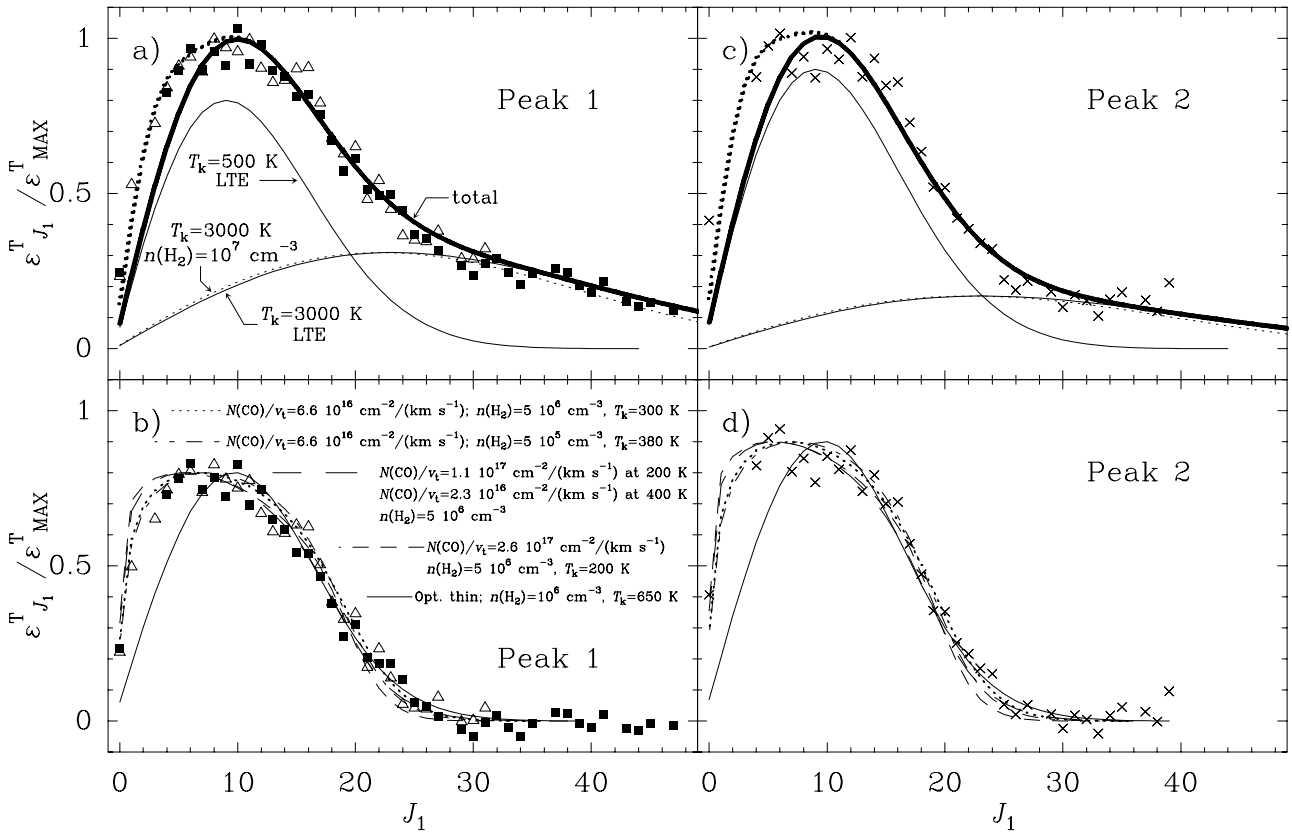

Fig. 7. Predicted and observed J_1-distributions (**a)** and **b)**: Peak 1; **c)** and **d)**: Peak 2) of the total flux arising in the $P-$ and $R-$lines that have a common (v = 1, J_1) level. Symbols have the same meaning as in Fig. 3. **a)** and **c)** Solid thin lines show results for the warm and hot components in the optically thin limit and assuming LTE. The distribution of the total flux, calculated by adding the fluxes from both T_k-components, is indicated by the solid thick line. The dashed thick line is the result of including a third (cold) T_k = 50 K component to match the flux of the low-J_1 lines. The dotted thin line displays the expected distribution in NLTE for the hot component by assuming $n(H_2) = 10^7$ cm^{-3}. **b)** and **d)** Observed distribution after subtracting the predicted fluxes of the hot component (solid thin line in panel a for T_k = 3000 K). The different curves show the predicted distributions in NLTE for various labelled physical conditions (see text for details).

in Eq. (10). The J_1-dependence of σ accounts for deviations of the $v = 0$ populations from the Boltzmann distribution. If the density is large enough to thermalize the $v = 0$ levels, then

$$\sigma^* = n_c n_{0,0} \sum_{J_3} g_{J_3} k_{1,J_3 \rightarrow 0,0} \qquad (11)$$

does no longer depend on J_1; henceforth the distribution of $\epsilon^T_{J_1}$ with J_1 is expected to be, within the IOSA, purely a Boltzmann distribution, independent of the specific values of $k_{1,J\rightarrow 0,0}$. For low J_1, $E^{rot}_{1,J_1} \ll kT_k$ and the pump rate per magnetic sublevel becomes also independent of angular momentum. This result was found by Watson et al. (1980) and Elitzur (1980) and applied to the study of the collisional pumping of SiO masers in the innermost regions of evolved stars. The more moderate densities that may prevail in shocked regions will require in the present case the estimate of the J_1 dependence of σ. For this purpose, we use the SiO-He *relative* values of $g_{J_3} k_{1,J_3\rightarrow 0,0}$ (BG). Following DePristo et al. (1979), approximate corrections for the finite duration of the collision can be done by inserting in the J_2 summation of Eq. (10) the adiabatic factor

$$\left| A^{1,J_1;0,J_2}_{1,J_3} \right|^2 = \left[\frac{E_{1,J_3} - E_{0,J_3-1+\delta_{J_3,0}}}{E_{1,J_1} - E_{0,J_1-sign(J_1-J_2)}} \right]^4 , \qquad (12)$$

where $sign(J_1 - J_2)$ is 1, 0 or -1 for $J_1 > J_2$, $J_1 = J_2$, and $J_1 < J_2$, respectively. In Eq. (12) we have applied the adiabatic limit (DePristo et al. 1979), appropriate to both H_2-CO and H-CO collisions for $T_k \leq 3000$ K. The results obtained with the application of this correction are, nevertheless, very similar to those obtained without it.

Figure 8 compares the observed distribution of $F^P_{J_1} + F^R_{J_1}$ in Peak 1 with that predicted from Eqs. (9) and (10). The latter is independent of the total rate coefficient for CO $v = 0-1$ excitation because the calculated distribution is normalized. From the discussion above, it is evident that the LTE results are the same as in the case of radiative pumping. For $n(H_2) = 10^6$ cm^{-3}, results are also very similar to those of Fig. 7b in the optically thin limit, yielding T_k of ∼650 K. The most important differences between radiative and collisional pumpings are obtained in models where the ro-vibrational lines are optically thick.

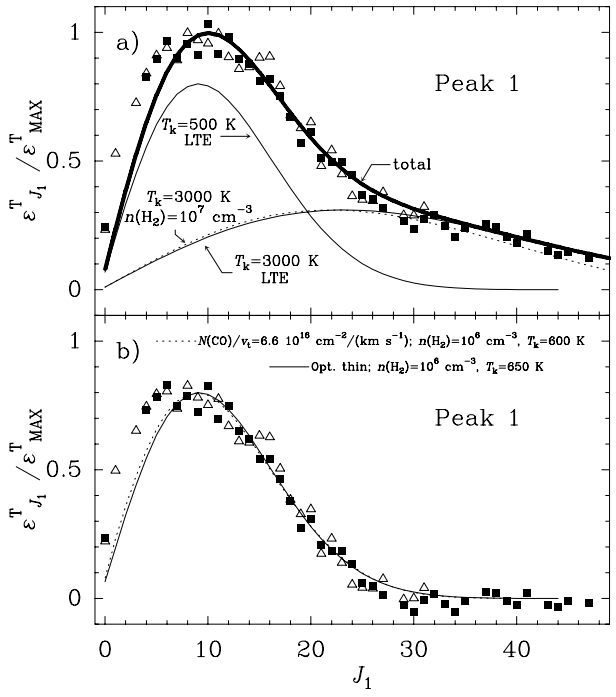

Fig. 8. Same as Figs. 7a,b but for collisional pumping (Peak 1).

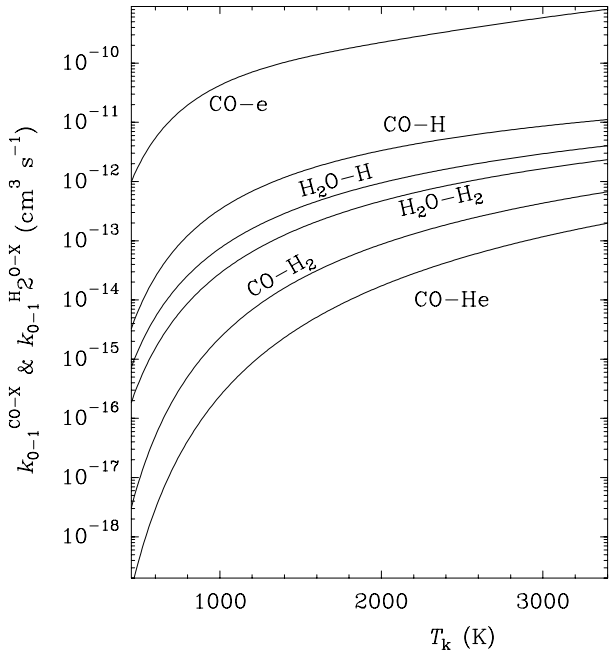

Fig. 9. Rate coefficients for CO $v = 0-1$ excitation through collisions with electrons, atomic hydrogen, molecular hydrogen, and helium, and for H_2O $\nu_2 = 0-1$ excitation through collisions with atomic and molecular hydrogen. CO curves show fits to experimental data, and are reported by Draine & Roberge (1984) for CO-e, Glass & Kironde (1982) for CO-H, and Millikan & White (1963) for CO-H_2 and CO-He. H_2O curves are based in Eq. (13).

For collisional excitation, opacities significantly larger than unity hardly modify the width of the distribution (dotted line in Fig. 8b), so that the relative fluxes of the low J_1 lines are always underestimated. The addition of a component with lower T_k cannot solve this discrepancy because of the very low values of the collisional rates at low T_k (Sect. 4.2.1). According to the relative enhancement of the low-J lines at Peak 2, this conclusion is also applicable to the CO band at this position.

In Sect. 4.2.2 we show that only CO-H collisions in (partially) dissociative shocks could have some observable effects on the CO $v = 1-0$ emission; collisions with H_2 can be ignored because of their low translational to vibrational energy transfer efficiency. A high atomic hydrogen fraction will affect in general the distribution of populations in the $v = 0$ state and also the relative values of $g_{J_3}k_{1,J_3\rightarrow 0,0}$, but none of these will modify, within the IOSA approach, the T_k derived above if the $v = 0$ populations have nearly a Boltzmann distribution. Green & Thaddeus (1976) have shown that collisional rates for rotational transitions at 100 K for CO-H are lower than for CO-H_2, but at higher temperatures results are uncertain due to the presence of resonances in CO-H rotational inelastic scattering that are a consequence of the formation of the HCO intermediate complex (Lee & Bowman 1987). On the other hand, experimental studies of the CO $v = 1$ rotational distribution in CO-H collisions have been only performed for well defined and high kinetic energies of H and low rotational temperatures of CO (e.g., Wight & Leone 1983; Chawla et al. 1988; McBane et al. 1991), so that thermal averages cannot be derived from these data. Theoretical efforts to fit those measurements underestimate the populations of low J in $v = 1$ relative to those of higher J (McBane et al. 1991; Kim & Micha 1989; Green et al. 1996). Nevertheless, these discrepancies should not affect the rotational distributions obtained in the present analysis, which is based on thermal averages.

For the warm component, the kinetic temperature we derive in the optically thin limit for both types of pumping, $T_k \sim 650$ K, coincides with other determinations that are based on observations of CO pure rotational lines (Watson et al. 1985; Sempere et al. 2000). However, this coincidence is surely fortuitous, because those pure rotational lines have been observed with larger beams that cover most of the OMC-1 shock, and arise from the low-velocity flow. In fact, the best match to the observed band shape is found in the case of radiative pumping and significant CO column densities (Figs. 7b and d), for which $T_k \sim 300$ K.

4.2. Radiative versus collisional excitation

4.2.1. Collisional pumping rates

Figure 9 plots k_{0-1}^{CO-X}, the CO excitation rate into the $v = 1$ state through collisions with partners X = e, H, H_2, and He. These curves are all based on laboratory data. Experimental measurements of $k_{0-1}^{CO-H_2}$ and k_{0-1}^{CO-He} are available from the works of Hooker & Millikan (1962) and Millikan & White (1963), who showed that these systems follow, like a variety of others, a systematic trend with T_k

that is readily explained in terms of the Landau-Teller theory. The absolute values of the vibrational relaxation time for these systems were satisfactorily accounted for by a single empirical equation, i.e.,

$$\ln(p\tau_v) = 1.16\times10^{-3}\mu^{1/2}\theta^{4/3} \times\left(T_{\rm k}^{-1/3}-0.015\mu^{1/4}\right)-18.42, \quad (13)$$

where p is the partial pressure of the collisional partner in atm, $\tau_{\rm v}$ is the relaxation time in seconds, μ is the reduced mass of the system in atomic mass units, and θ is the characteristic temperature of the oscillator in K. Application of this general equation to the CO-H_2 and CO-He systems yields for the de-excitation rates (Thompson 1973; Draine & Roberge 1984)

$$k_{1-0}^{\rm CO-H_2} = 4.5\times10^{-14}T_{\rm k}\exp\{-68/T_{\rm k}^{1/3}\}\ {\rm cm^3\,s^{-1}}, \quad (14)$$

and

$$k_{1-0}^{\rm CO-He} = 1.0\times10^{-13}T_{\rm k}\exp\{-99/T_{\rm k}^{1/3}\}\,{\rm cm^3\,s^{-1}}. \quad (15)$$

Equations (14) and (15) are valid for $T_{\rm k}$ above ∼200 K; at lower temperatures deviations from these formula are observed (Miller & Millikan 1970). These results may also be confirmed in the light of more recent measurements and calculations. Reid et al. (1997) have studied theoretically the relaxation times for vibrational deactivation of CO $v = 1$ by ortho-H_2 and para-H_2 at temperatures below 300 K, and found satisfactory agreement with the available experimental data. Since they provide monoenergetic cross sections for CO-$H_2(J)$ with $J = 0$, 1, and 2, rate constants $k_{1-0}^{\rm CO-H_2}$ at $T_{\rm k}$ above 300 K can be estimated by extrapolating those cross sections and performing then the average over the kinetic energy distribution (see also Ayres & Wiedemann 1989). This extrapolation is justified because at $T_{\rm k}$ above ≈160 K the rate constants are dominated by ballistic collisions (Reid et al. 1997). In this way we have checked that the extrapolated rate constants agree with the formula of Millikan & White (1963) within a factor of 2–3 for $T_{\rm k} \leq 1000$ K. This is of course merely indicative, but supports that the rate constants of Eq. (14) are not strongly underestimated. On the other hand, the translational to vibrational (T-V) energy transfer efficiency is much lower for CO-He, and these collisions can be ignored at this moment.

Experimental determinations of k for collisions with atomic hydrogen are much more scarce, but the few available data indicate values of two to three orders of magnitude larger than those corresponding to H_2. T-V energy transfer is enhanced due to the formation of the HCO intermediate complex. Vibrational relaxation probability for CO in collisions with H was first studied by von Rosenberg et al. (1974), but here we use the results of the subsequent experiments by Glass & Kironde (1982), which were performed over a wider temperature interval (840–2680 K) (see also Ayres & Wiedemann 1989):

$$k_{1-0}^{\rm CO-H} = 9.9\,10^{-15}T_{\rm k}\exp\{-3/T_{\rm k}^{1/3}\}\ {\rm cm^3\,s^{-1}}. \quad (16)$$

The Glass & Kironde results have been extrapolated to lower and higher temperatures in Fig. 9. On the other hand, excitation through collisions with electrons is still more efficient (Draine & Roberge 1984):

$$k_{1-0}^{\rm CO-e} = 1.9\times10^{-11}T_{\rm e}^{0.5}(\sqrt{2420/T_{\rm e}}+10\sqrt{1+10\,500/T_{\rm e}} \times\exp-10\,210/T_{\rm e})\ {\rm cm^3 s^{-1}}, \quad (17)$$

where $T_{\rm e}$ is the electron temperature (identified with $T_{\rm k}$ in Fig. 9). Nevertheless, it seems unlikely that a high electron density is present at Peak 1: although Hasegawa & Akabane (1984) claimed a possible detection of H51α in Orion-KL, Jaffe & Martín-Pintado (1999) do not find any broad component in their H39α spectrum toward Peak 1. Finally, we have assumed that Eq. (13) can be used to compute the rates for collisional excitation of the H_2O $\nu_2 = 1$ state. We obtain for H_2O-H_2 collisions,

$$k_{1-0}^{\rm H_2O-H_2} = 3.1\times10^{-14}T_{\rm k}\exp\{-47.1/T_{\rm k}^{1/3}\}\,{\rm cm^3\ s^{-1}}, \quad (18)$$

and for H_2O-H,

$$k_{1-0}^{\rm H_2O-H} = 2.3\times10^{-14}T_{\rm k}\exp\{-34.2/T_{\rm k}^{1/3}\}\,{\rm cm^3\ s^{-1}}. \quad (19)$$

4.2.2. Radiative to collisional pumping rate ratio

In Fig. 10 we compare the radiative and collisional pumping rates, for both the CO and H_2O bands, by displaying their ratio. Collisional rates for CO and H_2O are taken from Fig. 9. A density of 10^6 cm^{-3} has been adopted as a reference value for any considered collisional partner, H or H_2, but the curves in Fig. 10 can be easily scaled to other densities. H_2 preshock densities of *a few* $\times 10^5$ cm^{-3} have been derived from the H_2 line emission at Peak 1 by several authors (Draine & Roberge 1982; Chernoff et al. 1982).

The radiative pumping rates have been computed from Eq. (6) (i.e., in the optically thin limit) for CO (and similarly for H_2O) by assuming that the extinction at 4.7 and 6.5 μm is zero. The CO $v = 0$ populations have been assumed to follow a Boltzmann distribution at $T_{\rm k}$, but those of H_2O have been calculated by using the collisional rates of Green et al. (1993) and assuming $n(H_2) = 10^6$ cm^{-3}. However, we find that results are nearly independent of the distribution of populations in the ground vibrational state as long as all the ro-vibrational lines remain optically thin. Our choice of the stellar parameters attempts to simulate the flux of the stellar radiation in the mid-infrared at Peak 1, where the close and strong star BN is assumed to be the main excitation source. We follow the work of Lee & Draine (1985), who matched the intrinsic BN flux (i.e., once the observed flux from BN is corrected for the extinction by the quiescent cloud) between 2 and 10 μm by (*i*) a blackbody source with $T_{\rm s} \approx 1100$ K and $r_{\rm s} \approx 8.4\times10^{13}$ cm (at 450 pc), which represents the emission from optically thick dust surrounding BN, and (*ii*) an additional contribution from optically thin dust emission that becomes dominant at wavelengths longer than

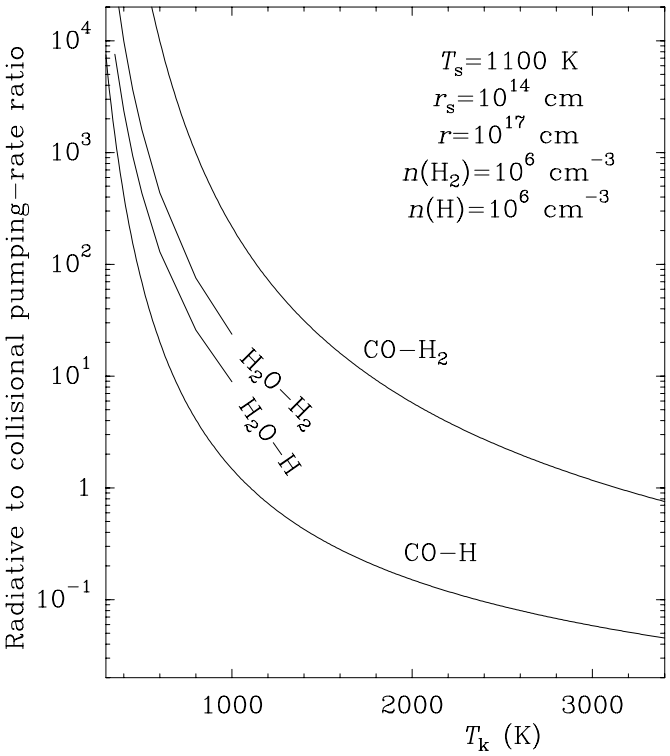

Fig. 10. Estimation of the radiative to collisional pumping rate ratio as a function of kinetic temperature. Rates of radiative excitation for CO have been computed from Eq. (6) (zero extinction is assumed) by summing over all $v = 1$ rotational levels, and similar expressions have been used for H_2O. Molecules are assumed to be located at $r = 10^{17}$ cm from the stellar source. Excitation through collisions with H_2 and H is considered, with assumed densities of 10^6 cm^{-3} for both cases.

$\sim$6 μm. We have ignored this last contribution, but compensate for the consequent underestimation of the stellar flux at 4.7 μm by increasing r_s to 10^{14} cm. The stellar flux at 6.5 μm is then still underestimated by a factor of $\approx$1.5. The adopted distance between BN and the CO molecules, $r = 10^{17}$ cm, corresponds to the observed angular distance between BN and Peak 1 (15″) at 450 pc. Our simulation of the radiation field at Peak 1 is only tentative, since apart from the intrinsic uncertainty in the BN model by Lee & Draine (1985), (*i*) we implicitly assume isotropic emission from the dust surrounding BN, (*ii*) we assume that the extinction between BN and Peak 1 at 4.7 and 6.5 μm is zero, (*iii*) we ignore the possible significant contribution from other infrared sources in the region, (*iv*) there will be a range of distances r within the ISO/SWS beam, and (*v*) line opacity effects are not taken into account. Points (*iv*) and (*v*) are further discussed in Sects. 4.2.3 and 4.2.4. We estimate that the uncertainty associated with the computed radiative pumping rates may be as large as a factor of 4.

Despite of this, a number of conclusions can be drawn from Fig. 10: 1) Collisions with H_2 can be completely ignored in the warm component as compared with the estimated radiative excitation rates. 2) A very high atomic hydrogen density in the warm component ($T_k \approx 500$ K) is needed to compete with radiation in pumping the excited v-states of both CO and H_2O ($\sim 5 \times 10^7$ cm^{-3} for CO and $\sim 5 \times 10^8$ cm^{-3} for H_2O). 3) For the hot component, collisions with both H_2 and H are presumably more efficient than radiation, according to the fact that densities of at least 10^7 cm^{-3} are necessary to explain the rotational distribution for $T_k = 3 \times 10^3$ K (otherwise higher T_k should be invoked).

Concerning Peak 2, the main source of radiative excitation is most probably located in the vicinity of IRc2, but the intrinsic flux from this source is more difficult to quantify. Gezari et al. (1998) showed that IRc2 itself is not the dominant luminosity source in the region, and suggested that the hot star(s) that ionize the compact HII region "I", which is displaced 0.″8 from IRc2 and is coincident with the SiO maser, could account for most of the luminosity from Orion BN/KL. Source "I" may be heavily obscured by the intervening hot core, which has $\tau \sim 0.05$ at 3.5 mm (Wright et al. 1992) and could have $\tau > 5$ at 20 μm (Gezari et al. 1998), thus explaining the lack of a strong point-like emission at the "I" position in the mid-infrared images of BN/KL (Gezari et al. 1998). If the dust cocoon around this star (where the SiO maser emission arises) has a temperature of $\sim 10^3$ K and a radius of $\sim$0.″05 (3.4×10^{14} cm) (Gezari et al. 1998), and the hot core does not block the radiation emitted from that cocoon in the direction of Peak 2, the unattenuated 4.7 μm continuum flux at the position of Peak 2 (at 2×10^{17} cm from source "I") will be twice the continuum flux at Peak 1 as calculated from the model for BN described above. In such a case, the intensity of the radiation field in the mid-infrared at Peak 1 would be also dominated by the emission from source "I" (rather than from BN), thus accounting for the similarities between the CO and H_2O band fluxes at both positions.

The above estimate is however very uncertain, and mainly has the purpose of showing that the radiative pumping of the CO $v = 1$ and H_2O $\nu_2 = 1$ states at Peak 2 may be as efficient as at Peak 1. Given that the band shapes and fluxes are very similar at both peaks, we will assume that the conclusions on the relative importance of radiative and collisional pumping (based on differences of orders of magnitude) are also applicable to Peak 2, and for simplicity we will further assume that the parameters T_s, r_s, and r in Fig. 10 can be also used to characterize approximately the continuum intensity at Peak 2.

4.2.3. Column densities for the warm component in the optically thin limit

If the excitation of the CO $v = 1$ state were collisional, the beam averaged CO column density N(CO) would be related to the observed flux by

$$N(\mathrm{CO}) = \frac{4\pi\lambda}{hc\Omega_\mathrm{B}} \frac{10^7 F_\mathrm{CO}^{v=1-0}(\mathrm{Wcm^{-2}})}{n(\mathrm{X}) k_{0-1}^{\mathrm{CO-X}}} \ \mathrm{cm^{-2}}, \qquad (20)$$

where X is the collisional partner, λ is the average wavelength of the emitted photons, and $k_{0-1}^{\mathrm{CO-X}}$ is the total

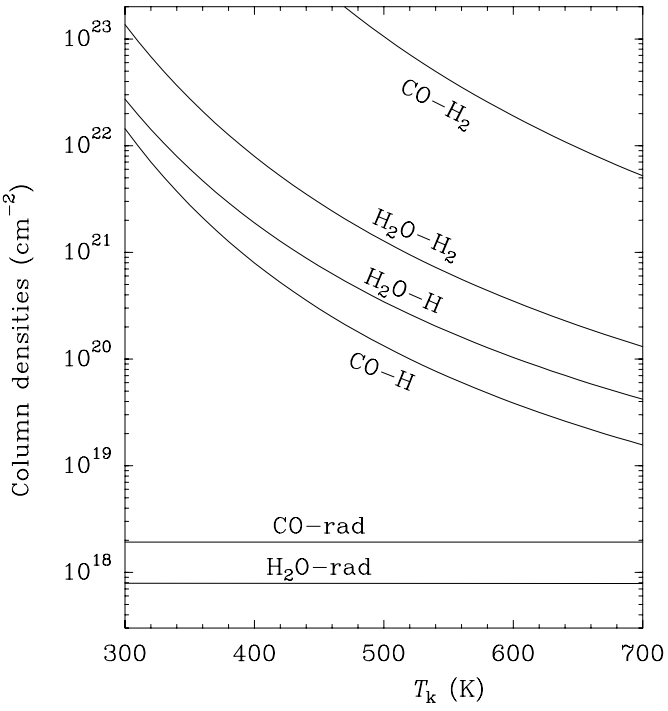

Fig. 11. Beam averaged CO and H_2O column densities required to explain the observed fluxes toward Peak 1 from the warm component through collisions with H_2 (CO-H_2 and H_2O-H_2 curves), collisions with H (CO-H and H_2O-H), and resonant scattering (CO-rad and H_2O-rad). Densities of 10^6 cm^{-3} have been assumed for both H_2 and H. Calculations for resonant scattering assume that the ro-vibrational lines are optically thin, and the parameters T_s, r_s, and r are those of Fig. 10. Since band fluxes are very similar at both peaks, these results can be also applied to Peak 2.

rate for excitation into the CO $v = 1$ state. Equation (20) is valid also for optically thick emission, provided that A/τ remains much larger than the rate for collisional de-excitation from $v = 1$ to the ground state. If the ro-vibrational lines are optically thick, line photons will be scattered several times before leaving the cloud, but with little chance of being thermalized by a collisional de-excitation event. Finally, Eq. (20) assumes isotropic emission. On the other hand, if the pumping were radiative, and the ro-vibrational lines were optically thin, an expression similar to that of Eq. (20) is valid with the substitution of $n(\mathrm{X})k_{0-1}^{\mathrm{CO-X}}$ by the corresponding radiative pumping rate per molecule (the parameters T_s, r_s, and r are those of Fig. 10). Similar expressions are also used for H_2O.

Figure 11 shows that, for the warm component, the column densities that must be invoked to explain the CO and H_2O fluxes from Peak 1 through excitation by collisions are very large for the assumed H density of 10^6 cm^{-3}. Only a very high density of atomic hydrogen ($\sim 5 \times 10^7$ cm^{-3}) could reduce N(CO) to acceptable levels, but still the band shape would be difficult to explain (Sect. 4.1.2). In a strong J-shock (HM; Neufeld & Dalgarno 1989), molecular reformation follows the formation of H_2 and, although still an important fraction of CO may coexist with significant amounts of atomic hydrogen, H_2O is formed after the reformation of H_2 is almost complete and its abundance remains more than one order of magnitude lower than that of CO. This prediction disagrees with our observations. C-shocks can be also disregarded because of their low dissociation fraction. Therefore it is very unlikely that collisions pump the excited v-states of CO and H_2O in the warm component. This result also applies to Peak 2, given that the band fluxes and shapes are very similar at both positions.

On the contrary, the assumption of resonant scattering yields significantly lower (although still large, Sect. 4.2.4) column densities at Peak 1, nearly independent of T_k. Effects of line opacities, discussed below, show that N(CO) and $N(H_2O)$ in Fig. 11 may be underestimated by factors of 3 and 2, respectively. Nevertheless, the main source of uncertainty is the intensity of the radiation field. The assumption of zero extinction between BN and Peak 1 could also lead to an underestimate of N(CO, H_2O), but may be supported by the cavity-model for Orion-KL proposed by Wynn-Williams et al. (1984). On the other hand, the distance $r = 10^{17}$ cm between BN and the emitting CO molecules could be somewhat overestimated: GG showed that the spatial distribution of the CO $P(8)$ line in Peak 1 is quite different from that of the H_2 $S(1)$. The $P(8)$ line was found to peak along a narrow "ridge", which is closer to BN ($10''$ or 7×10^{16} cm) than Peak 1 and seems to extend further in the direction of BN. This ridge, although close to the edge of the SWS aperture, lies within it. It is also worth noting that, since H_2 is excited through collisions (RBD), the assumption of different excitations mechanisms for CO and H_2 readily accounts for the above difference in their spatial distributions. Regarding Peak 2, it is further from IRc2 than Peak 1 from BN, but Geballe (1993) showed that there are also striking differences in the spatial distributions of H_2 and CO at this position: several CO ro-vibrational lines were found to be as strong as the H_2 $S(9)$ line $10''$ north from Peak 2, i.e., closer to IRc2 and BN.

Two additional observational facts show the ability of IRc2 and BN to excite the CO $v = 1$ and H_2O $\nu_2 = 1$ states through radiative pumping. First, the P-Cygni profiles of most CO P(J) lines observed toward IRc2 (Fig. 1) are a strong indication of radiative pumping. Second, we reported in González-Alfonso et al. (1998) that the H_2O band toward BN shows the $R-$branch in absorption and the $P-$branch in emission. This absorption/emission pattern was readily explained in terms of radiative pumping. The fact that the emission in the $P-$branch was found to be stronger than the absorption in the $R-$branch was primarily ascribed to some contribution from a region where the H_2O $\nu_2 = 1$ state is pumped through collisions, although deviations from spherical symmetry around BN could also account for it. In view of the present observations and analysis, we conclude that deviations from spherical symmetry, which are the consequence of the extension of the flow in the plane of the sky, are most

probably producing the excess of emission in the H_2O $P-$branch toward BN.

An additional point supports the possibility that the CO $v = 1-0$ emission from the warm component in OMC-1 is radiatively pumped: Grasdalen et al. (1992) showed that the CO band emission is correlated with the continuum in the near infrared. Given the lack of stellar sources at the observed positions, and that the continuum at 4.5–5 μm in Peak 1 (Fig. 1) seems bluer than the BN intrinsic spectrum inferred by Lee & Draine (1985), the observed continuum is supposed to originate from scattering by dust. Thus the above correlation is readily explained if both the CO vibrational emission and the dust emission at the same wavelengths are caused by scattering.

Accepting that resonant scattering is responsible for the observed emission, Fig. 11 also indicates that the beam-averaged N(CO) is a factor of >2 larger than $N(H_2O)$. This result does not depend on T_k nor on the luminosity of the stellar sources. Under the assumption that the stellar spectrum in the direction of Peak 1/2 can be characterized by effective temperatures not much larger than $T_s = 1100$ K, the following considerations further indicate that CO is more abundant than H_2O: (*i*) effect of line opacities will modify by a similar factor the inferred column densities of CO and H_2O (Fig. 13); (*ii*) the extinction $\mathcal{A}_\lambda$ along the path that connects BN and IRc2 with Peak 1 and Peak 2, if significant, can be expected to be larger at 4.7 than at 6.5 μm, leading to a larger CO abundance relative to that of H_2O; (*iii*) assuming isotropic emission from BN, in the model of Fig. 11 the BN flux at 6.5 μm is underestimated in relation to the flux at 4.7 μm, because of the additional contribution of optically thin dust emission at 6.5 μm (Fig. 7 of Lee & Draine 1985).

4.2.4. Opacity effects and abundances

Opacity effects have been tested with the radiative transfer code described in González-Alfonso & Cernicharo (1997, 1999). A sketch of the model source is given in Fig. 12. Following Draine & Roberge (1982), the Orion shock front is idealized as a spherical shell of gas with inner and outer radii of 2×10^{17} and $r_M = 2.1\times10^{17}$ cm, respectively. The outer radius corresponds to 30″ at 450 pc, so that the OMC-1 infrared cluster should be located around the center of the sphere. The ISO/SWS beam is centered at Peak 1/2, so that only the region above the horizontal plane is supposed to be covered by the beam. The z-coordinate of this plane is defined as $f_b \times r_M$. If $f_b = 0.7$, the spherical cocoon above the plane subtends a solid angle equal to that of the ISO/SWS beam (6.6×10^{-9} sr). In such a case, and according to the contribution by the near and far sides and to the curvature of the shell, the beam-averaged column density is ≈5.7 times the radial column density.

In order to avoid those opacity effects that are the consequence of the spherical symmetry, the radiation from BN/IRc2 and the rest of the infrared sources is represented as a background isotropic source with $T_s = 1100$ K and diluted by the geometrical factor $\pi r_s^2/r^2$, where $r_s = 10^{14}$ cm and $r = 10^{17}$ cm. The corresponding continuum intensity is multiplied by the factor f_s, which accounts for the uncertainties regarding the stellar flux in the infrared and the distance r (Sects. 4.2.2 and 4.2.3).

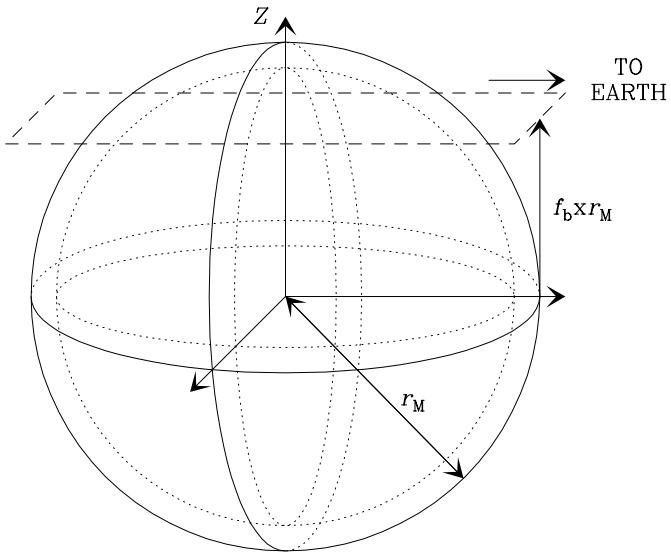

Fig. 12. Schematic representation of the modelled source, which is a spherical shell of gas with outer radius $r_M = 2.1\times10^{17}$ cm and inner radius of $r = 2\times10^{17}$ cm. Only the emission from the spherical cocoon above the dashed horizontal plane (with z coordinate $f_b \times r_M$) is observed with the ISO/SWS beam. The column density calculated along the direction of the observer and averaged over this cocoon defines the beam-averaged column density.

In Fig. 13, solid lines show the predicted CO and H_2O fluxes for "pure microturbulent" models (Sect. 4.1.1) and assuming $f_s = 1$. For the adopted $v_t = 20$ km s^{-1}, the calculated HPW of the CO $P(8)$ line is 50–70 km s^{-1} for CO column densities larger than $\approx3\times10^{18}$ cm^{-2}. The results of Fig. 13 indicate that the column densities required to explain the observed CO and H_2O band fluxes are factors of ≈3 and ≈2 times, respectively, larger than those obtained in the optically thin limit (Fig. 11). Other characteristics of the models are the following: (*i*) Predicted band fluxes are modified by less than 25% for CO and by less than 40% for H_2O if $n(H_2)$ is decreased by one order of magnitude or T_k is increased up to 600 K; (*ii*) band fluxes are nearly independent of the geometrical parameters (r_M and the width of the shell) as long as f_b is varied so that the solid angle subtended by the source remains equal to the SWS beam; (*iii*) band fluxes are proportional to f_s; (*iv*) if v_t increases, line opacities decrease and solid lines in Fig. 13 approach the optically thin results (dashed lines); (*iv*) if the observed linewidths are primarily broadened by a systematic – expanding – velocity field, the velocity dispersion in the radial direction decreases, and therefore larger column densities (or larger f_s) are required to explain the observed fluxes.

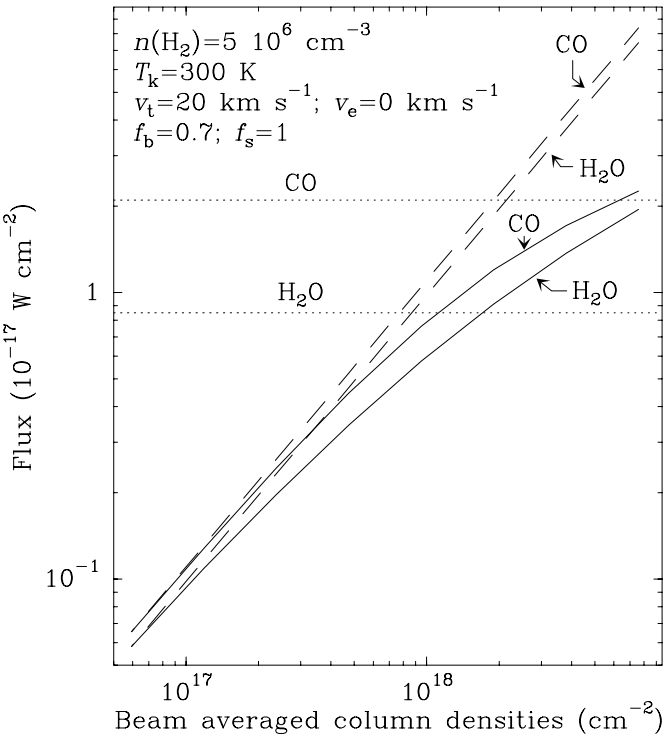

Fig. 13. CO $v = 1{-}0$ and H_2O $\nu_2 = 1{-}0$ total fluxes versus beam-averaged column densities. Solid lines display the results of models that include opacity effects (Sect. 4.2.4). The solid angle subtended by the source is equal to that of the ISO/SWS beam ($f_b = 0.7$; see text). Dashed lines indicate the linear relationship that would hold if the ro-vibrational lines were optically thin. Horizontal dotted lines indicate the observed fluxes from the warm component toward Peak 1 (values for Peak 2 are similar).

The derived beam-averaged N(CO) of $\approx 6\times10^{18}$ cm^{-2}, which corresponds to a radial N(CO) of $\approx 10^{18}$ cm^{-2}, is similar to the value inferred from the observed band shape (Sect. 4.1.1). High N(CO) along the line of sight (at least 5×10^{18} cm^{-2}) are also needed to match the observed P-R-asymmetry, discussed in Sect. 4.4.2. These three estimations are consistent and independent of each other, but are not consistent with the H_2 column densities observed in the same beam. At Peak 1 and 2, the beam-averaged $N(H_2)$ *above* 200 K does not exceed $\approx 1.3 \times 10^{22}$ cm^{-2} (RBD; Wright 2000), which imposes an upper limit for the beam-averaged N(CO) of $\approx 3.5 \times 10^{18}$ cm^{-2} (we use the gas-phase C/H ratio of 1.4×10^{-4} derived by Sofia et al. 1997). If the H_2 0–0 S(1) line, with upper level column densities of $\approx 5.5 \times 10^{20}$ cm^{-2} at Peak 1 (RBD) and $\approx 3.3 \times 10^{20}$ cm^{-2} at Peak 2 (Wright 2000), is assumed to arise *entirely* from a region at 200 K, the consequent *strong* upper limits for N(CO) will be 6.3×10^{18} cm^{-2} and 3.7×10^{18} cm^{-2} for Peak 1 and Peak 2, respectively, but they will decrease by a factor of $\approx$3.7 if T_k rises to 300 K, which is the best T_k estimate for the warm component. It is also interesting to compare the intensity predicted for the CO $v = 0$ $J = 2{-}1$ pure rotational line with that observed at Peak 1. For N(CO) $= 6 \times 10^{18}$ cm^{-2}, $\Delta v = 50$ km s^{-1} and $T_k = 200$–300 K, the opacity of the CO $v = 0$ $J = 2{-}1$ line is 0.28–0.12 and the peak brightness temperature is 50–34 K. These values are still compatible with the peak antenna temperature at Peak 1 of $\approx$50 K (once the contribution from the quiescent cloud has been approximately subtracted), as measured by Rodríguez-Franco et al. (1999) at offset position $(-12'', 24'')$ from IRc2. Nevertheless, the above N(CO) may be also considered a strong upper limit because the emission in the CO $v = 0$ $J = 2{-}1$ line is probably dominated by gas components with temperatures lower than 200 K.

We find two possible solutions to this conflict. First, we may assume that f_s is significantly larger than 1 (i.e., $f_s = 2$–3). The beam-averaged column densities inferred from Fig. 13 would decrease as $f_s^{-1} - f_s^{-2}$ (depending on the opacity). Since still large *source-averaged* column densities are required to explain the band shape and the P-R-asymmetry, it follows that significant beam-filling would affect the observed emission. Therefore one would conceive the emitting source within the ISO/SWS beam as long and discreet tongues of gas nearly aligned along the line of sight, or a shell fragmented into structures that are primarily elongated in the direction of the observer. This scenery may find support in the observations of GG, who showed that the emission of the CO $P(8)$ line is unevenly distributed around Peak 1, and in the NICMOS image of the region (Stolovy et al. 1998), showing a small-scale clumpy structure in the emission of the H_2 $v = 1{-}0$ $S(1)$ line. A clumpy structure has been also observed by Vannier et al. (2001) around Peak 2. Second, the possibility that a substantial fraction of hydrogen is in atomic form cannot be disregarded (see RBD).

These considerations also lead to the conclusion that relatively large densities (at least 5×10^6 cm^{-3}) are involved in the observed CO and H_2O emission at both peaks. Lower densities would imply higher temperatures to match the CO band shape (Sect. 4.1.1) and, since the H_2 column density decreases strikingly with T_k (RBD; Wright 2000), a stronger discrepancy would be found between the CO and H_2 column densities. The analysis of the H_2O band in Sect. 4.4.3 confirms this point.

4.2.5. The CO column density in the hot component

The CO emission from the hot component at Peak 1 cannot be reconciled with the H_2 column densities reported by RBD if (*i*) collisions with H_2 are assumed to be responsible of the CO $v = 1$ excitation, and (*ii*) $n(H_2)$ is significantly lower than $\sim 3 \times 10^8$ cm^{-3}. For reference: using Eq. (20) with $n(H_2) = 10^7$ cm^{-3} and $T_k = 3 \times 10^3$ K, we find N(CO) $\approx 1.8\times10^{17}$ cm^{-2}, to be compared with $N(H_2)$ of 2.4×10^{19} cm^{-2} for $T_k \geq 1800$ K (RBD). Also, in Sect. 4.3 we estimate that, at least in the framework of current C-shock models, it is very unlikely that this component has its origin in ambipolar diffusion. Therefore, an H_2 density

of at least 3×10^8 cm^{-3} and $T_k \sim 3 \times 10^3$ K are involved or, alternatively, these extreme physical conditions can be partially relaxed by assuming that atomic hydrogen with relatively high densities coexists with CO in the hot component pumping its $v = 1$ state. With $n(H) = 10^7$ cm^{-3} and $T_k = 3 \times 10^3$ K, we derive $N(CO) \approx 9 \times 10^{15}$ cm^{-2}. The H_2 dissociation fraction will be given by

$$X_D = 1 - X(CO)\frac{N(H_2)}{N(CO)}, \quad (21)$$

where $X(CO)$ is the CO abundance relative to half of the hydrogen nuclei, and excitation through collisions with H_2 is assumed to be negligible (i.e., H_2 densities are significantly lower than 3×10^8 cm^{-3}). Adopting again $N(H_2) = 2.4 \times 10^{19}$ cm^{-2}, and $X(CO) = 2 \times 10^{-4}$, we obtain an H_2 dissociation fraction larger than 40%. These numbers are merely indicative, but strongly suggest that a component with high density, temperature, and perhaps dissociation fraction, is at the origin of the high-J CO ro-vibrational lines and, at least partially, also at the origin of the H_2 emission from the highest energy levels.

Sempere et al. (2000) found in the ISO/LWS spectrum of IRc2 CO pure rotational lines up to $J_{up} = 43$, indicating the presence of a high temperature component. Confusion in the LWS grating spectrum by lines of other species was critical, but the fluxes of the lines around $J_{up} = 40$ could be estimated to be $\sim 10^{-17}$ W cm^{-2}. We have checked that the hot component observed in the CO ro-vibrational lines could also account for that emission. Since all the strong H_2 sources in Orion BN/KL are located within the LWS beam ($\approx 70''$), with regard to Fig. 12 we compute the fluxes of the pure rotational lines from the whole spherical shell ($\approx 60''$ diameter). Adopting a radial $N(CO) = 1.6 \times 10^{15}$ cm^{-2} (corresponding to a source-averaged $N(CO) = 9 \times 10^{15}$ cm^{-2} within the spherical cocoon of Fig. 12), $T_k = 3 \times 10^3$ K, and $n(H) = n(H_2) = 10^7$ cm^{-3}, the predicted fluxes for the lines around $J_{up} = 40$ are $\approx 10^{-17}$ W cm^{-2}, as observed. The contribution from the spherical cocoon in Fig. 12 (with $f_b = 0.7$) is $\approx 0.2 \times 10^{-17}$ W cm^{-2}. Results are similar if $n(H) = 0$ and $n(H_2) = 3 \times 10^8$ cm^{-3} are adopted.

4.3. Nonthermal collisions with H_2

Ambipolar diffusion must be also considered as a possible excitation mechanism of CO $v = 1$ in the hot component. In a $C-$type shock, charged dust grains and ions drift through the neutrals and momentum transfer from magnetic field to the neutral gas takes place as a consequence of the resulting non-thermal high-velocity collisions (Draine 1980; Draine et al. 1983). After an ion-neutral collision occurs, the accelerated neutral particle generates a collisional cascade, so that most of the streaming collisions take place among neutral particles. Nonthermal collisions are predicted to be responsible for some degree of dissociation in an MHD shock (Draine & Roberge 1982; Chernoff et al. 1982), and also of enhanced excitation of high energy ro-vibrational levels of H_2 (O'Brien & Drury 1996). RBD have suggested that this may be an important mechanism for the emission from high-lying lines of H_2 in Peak 1.

We can roughly estimate the importance of this process in exciting the $v = 1$ state of CO as follows. Following O'Brien & Drury (1996), we assume that in a charge particle–H_2 or H_2–H_2 collision the velocity distribution of the collided H_2 is isotropic in the centre-of-mass frame. If the mass of the charged particle is much higher than that of H_2, the average velocity of H_2 after the (assumed elastic) collision in the laboratory frame (shock frame) is $\sqrt{2}v_d$, where v_d is the drift velocity between the charged and neutral components. For typical $v_d \sim 20$ km s^{-1}, the kinetic energy E_k^{ini} of the outcoming H_2 is ~ 8 eV. The subsequent collision cascade will distribute homogeneously this energy among the colliding H_2 particles. After n generations, the average E_k of the collided H_2 molecules is lower than the excitation energy of CO $v = 1$ ($E_{CO}^{v=1} = 0.26$ eV), so that CO-H_2 collisions in subsequent generations will not be able to excite the CO $v = 1$ state. In the first n generations, $2^n = E_k^{ini}/E_{CO}^{v=1}$ collisions have taken place, and the probability that one of them occurs between H_2 and CO is $X(CO)\sigma_{CO-H_2}/\sigma_{H_2-H_2}$, where $X(CO)$ is the CO abundance relative to H_2 and σ denotes the cross section of the collision. Therefore the rate of excitation of CO $v = 1$ by non-thermal collisions with H_2 is roughly

$$\frac{dn_{v=1}^{+}}{dt} = P_{01}X(CO)\frac{\sigma_{CO-H_2}}{\sigma_{H_2-H_2}}2^n n_i n(H_2) < \sigma v >_{i-H_2}, \quad (22)$$

where the subindex i refers to both charged dust grains and ions, and P_{01} is the translational-to-vibrational (T-V) energy transfer probability for CO $v = 1$ excitation in a CO-H_2 collision. This quantity should be considered some average over the kinetic energies available in the different generations. The predicted CO $v = 1{-}0$ flux observed in the ISO/SWS beam is $F_{CO}^{1-0} \sim 10^{-7} hc\Omega_B/(4\pi\lambda) \times dn_{v=1}^{+}/dt \times N(H_2)/n(H_2)$ W cm^{-2}.

According to Kaufman & Neufeld (1996b), we can characterize the coupling between the neutral and ionized (including dust grains) components by an ion-neutral coupling length L_{in} (which we estimate from their Fig. 1), so that

$$n_i < \sigma v >_{i-H_2} \sim \frac{v_d M_A}{L_{in}}, \quad (23)$$

where M_A is the neutral Alfvén Mach number. On the other hand, since T-V energy transfer probability P_{01} for monoenergetic CO-H_2 collisions are not available, we will use the results for CO-H collisions; they must be considered a strong upper limit due to the much higher efficiency for CO $v = 1$ excitation through CO-H than through CO-H_2 collisions (Fig. 9). Green et al. (1996) derived a cross section of 1.8 A^2 for CO $v = 1$ excitation in CO-H collisions at $E_k = 2.3$ eV, from which $P_{01} \sim 5 \times 10^{-2}$.

Adopting $P_{01} = 0.1$ we finally obtain

$$F_{\rm CO}^{1-0} \sim 1.4\times10^{-19}\left(\frac{\sigma_{\rm CO-H_2}}{\sigma_{\rm H_2-H_2}}\right)\left(\frac{P_{01}}{0.1}\right)\left(\frac{X({\rm CO})}{10^{-4}}\right) \times\left(\frac{M_{\rm A}}{10}\right)\left(\frac{N({\rm H_2})}{10^{22}\ {\rm cm^{-2}}}\right) \times\left(\frac{v_{\rm d}}{20\ {\rm km\,s^{-1}}}\right)^3\left(\frac{10^{16}\ {\rm cm}}{L_{\rm in}}\right) \quad (24)$$

in W cm^{-2}. If the terms in parenthesis are not much larger than unity, this is much lower than the observed flux in both the warm and the hot components. We thereby consider it unlikely that ambipolar diffusion has any significant effect on the observed CO $v = 1-0$ emission.

4.4. The P-R-asymmetry

4.4.1. General remarks

The P-R-asymmetry observed at Peak 1 and 2 in the CO $v = 1-0$ emission qualitatively resembles the general aspect of the H_2O $\nu_2 = 1-0$ band we observed with ISO toward Orion BN (González-Alfonso et al. 1998). We found that the $P-$branch was in emission while the $R-$branch was in absorption against the strong continuum of BN, and interpreted this effect as evidence of radiative pumping of the H_2O $\nu_2 = 1$ rotational levels. The simple 3-level system of Fig. 14, where levels 1 and 2 belong to the $v = 0$ state of the molecule and level 3 to the excited v state, accounts for this effect. We assume that Einstein coefficients and mean intensities are very similar for transitions 3–1 and 3–2. If level 3 is radiatively pumped, and if its population does not change in time, statistical equilibrium ensures that a net transfer of population via 1–3–2 takes place as long as the population per magnetic sublevel of level 1, n_1/g_1, is larger than that of level 2, n_2/g_2. The larger the difference $n_1/g_1 - n_2/g_2$ (i.e., the lower the rotational temperature), the more important the transfer of population will be. Since the 3–1 transition corresponds to the $R-$branch and the 3–2 to the $P-$branch, one may expect that in spherical symmetry (and if the source is not spatially resolved) the $R-$branch is observed in absorption and the $P-$branch in emission against the continuum of the central exciting source.

The possibility that some lines are observed in absorption relies of course on the location of the excitation source –BN in the present case- within the beam; since for both the Peak 1 and Peak 2 observations BN and IRc2 lie out of it, all the CO lines are observed in emission. However, the P-R-asymmetry suggests that an effect analogous to what was found toward BN in the H_2O $\nu_2 = 1-0$ band is also playing a role in the radiative transfer of the CO $v = 1-0$ lines that arise from the warm emitting region.

If the ro-vibrational lines are optically thin and in absence of a background source, it is easy to demonstrate that the P-R-asymmetry is negligible. In the system of Fig. 14, the fluxes of the $P-$ (3–2) and $R-$ (3–1) lines differ according to the different values of νA. For CO,

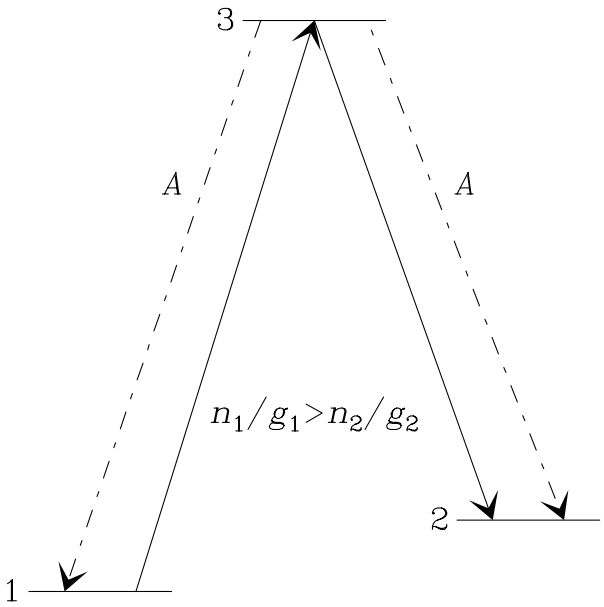

Fig. 14. 3-level molecular system that generally accounts for the P-R-asymmetry. The $v = 0$ rotational levels 1 and 2 are connected with the excited vibrational level 3 through $R-$ and $P-$transitions (dashed arrows), for which we assume similar Einstein coefficients. If the mean intensity is similar for both 3–1 and 3–2 transitions, the transfer of population 1–3–2 (solid arrows) will take place as long as the population per magnetic sublevel is larger for level 1 than for level 2.

the expected $F^P_{J_1}$ to $F^R_{J_1}$ ratio decreases with J_1, and the P-R-asymmetry becomes lower than 10% for $J_1 \geq 8$. This is contrary to what is observed.

If the lines are optically thick, line-emitted photons will be eventually absorbed by other CO molecules, allowing some 1–3–2 population transfer to take place. Following Sahai & Wannier (1985), the ratio of the flux of the $P(J_1 + 1)$ line to the $R(J_1 - 1)$ line is given by

$$\frac{F^P_{J_1}}{F^R_{J_1}} = \left(\frac{\nu^P_{J_1}}{\nu^R_{J_1}}\right)^4 \times \frac{n_{0,J_1-1}/g_{J_1-1}}{n_{0,J_1+1}/g_{J_1+1}}, \quad (25)$$

where we have assumed that the ro-vibrational lines are optically thick at all velocities within the line profiles, and that the population per magnetic sublevel of the $v = 1$, J_1 level can be neglected in comparison with the populations of the $v = 0$, $J_1 - 1$ and $J_1 + 1$ levels. Equation (25) implies that the relative fluxes of P and R lines with the same upper J_1 level only depend on the rotational temperature, $T_{\rm rot}$, in the $v = 0$ state (Sahai & Wannier 1985). For $T_{\rm rot} = 300$ K and J_1 ranging from 7 to 17, Eq. (25) yields flux ratios between 1.18 and 1.48 (in agreement with the models shown below). However, the observed fluxes in the warm component of both Peak 1 and 2, yield ratios larger than 1.5 (and most of them larger than 1.8). Lower rotational temperatures, of ∼150 K, are required to match the observed flux ratios, but a warmer component is needed to match the observed band shape. We conclude that, although optically thick emission is needed to account for the observed P-R-asymmetry, some other effects are

required to explain it quantitatively. Optically thick emission is consistent with the observations by GG, who found that the $P(8)$ line is considerably less peaked than the H_2 0–0 $S(9)$ line at Peak 1 and 2.

Wavelength-dependent extinction along the line of sight may account for some P-R-asymmetry, but it is appreciable only for sufficiently large J_1 (>15). From the extinction curve of RBD we estimate that the fluxes at 4.4 and 5 μm are attenuated by factors of 1.3 and 1.2, yielding a P-R-asymmetry lower than 8% for the lines that trace the warm component. On the other hand, column densities of hydrogen nuclei within the emitting source may be $\sim 5 \times 10^{22}$ cm^{-2} (for $N(\mathrm{CO}) \sim 7 \times 10^{18}$ cm^{-2} – Fig. 13 – and a CO abundance relative to H nuclei of 1.4×10^{-4}), from which the extinction at 4.7 μm will be ∼2.5 mag (we assume $N_\mathrm{H} = 2 \times 10^{21} \mathcal{A}_\mathrm{V}$ and $\mathcal{A}_\lambda \sim \lambda^{-1}$). If all the dust is assumed to be located in front of the gas, differential extinction across the band will account for a flux ratio of the $P(15)$ line to the $R(13)$ line of 1.13.

The observed continuum emission could enhance the observed P-R-asymmetry significantly. It provides a source of background that may play a role similar to that of a background stellar source. Consider a ray traveling in the direction of the observer. Both line photons and continuum at the right frequency will produce a net 1–3–2 transfer of population if the conditions outlined above are met. This transfer involves emission events in the $P-$branch and absorption events in the $R-$branch *relative* to that (observed) continuum; as pointed out above, the presence of a much more important source of excitation (the external radiation from BN/IRc2) will increase the fluxes of both branches and avoid the $R-$branch to be observed in absorption. The efficiency of dust scattering in enhancing the P-R-asymmetry depends on the relative location of dust grains and CO molecules, and will be the greatest if the dust is located behind CO, i.e., if the continuum photons provide a background source. This is not known, of course, and we assume in the models below that dust and CO are coexistent. On the other hand, the P-R-asymmetry is enhanced with larger $N(\mathrm{CO})$, because the line opacities increase and also because the value of T_k (and therefore the rotational temperatures) that fits the band shape decreases (Sect. 4.1).

4.4.2. Models for CO

Apart from the inclusion of dust, models in this section are the same as those described in Sect. 4.2.4. Photons scattered by dust are simulated simply by adopting an emissivity for grains with a temperature of 750 K (so that the continuum emission at 4.7 μm is nearly flat in units of Jy, as observed); the dust abundance is then fitted to match approximately the observed continuum flux. Dust emission enhances the P-R-asymmetry but only modifies by a few per cent the band fluxes.

Figure 15 shows some model predictions. For all them, a $T_\mathrm{k} = 3 \times 10^3$ K LTE model has been assumed for the hot component, and for the warm component $n(\mathrm{H_2}) = 5 \times 10^6$ cm^{-3}, and $f_\mathrm{b} = 0.7$ (the source fills the beam). At this density the relevant CO $v = 0$ rotational levels are nearly thermalized (Sect. 4.1.1), so that results for larger densities are nearly the same. The "pure microturbulent" model of panel a ($v_\mathrm{t} = 20$ km s^{-1}, and $v_\mathrm{e} = 0$ km s^{-1}) shows that, even for $N(\mathrm{CO}) = 7.5 \times 10^{18}$ cm^{-2}, the observed P-R-asymmetry is underestimated if dust is not taken into account. In panel b the effect of dust is included, and although the P-R-asymmetry increases significantly, it does not entirely account for the observed one despite the overestimation of the continuum flux (30 Jy against the observed continuum flux of 18 Jy). If the line widths are primarily broadened by an expanding velocity field (panel c), lower $N(\mathrm{CO})$ and T_k match the band shape but f_s must increase and the P-R-asymmetry is not reproduced. In panel d, two concentric shells of gas, at 230 K and 400 K, compose the modelled source. The P-R-asymmetry is better matched, but the required $N(\mathrm{CO})$ of $\approx 10^{19}$ cm^{-2} is a factor of ≈3 larger than the upper limit inferred from the H_2 emission (Sect. 4.2.4). If v_t increases, the dust effect is enhanced but, as shown in Sect. 4.1.1, $N(\mathrm{CO})$ must also increase to match the band shape. In the framework of our 1-D models, and taking into account the uncertainty concerning the subtraction of the flux from the hot component, we conclude that source-averaged CO column densities along the line of sight of at least 5×10^{18} cm^{-2} at 200–400 K are required to explain the P-R-asymmetry observed in the warm component, and that a beam filling factor of 2–3 (and/or a dissociation fraction of ∼50%) is also needed to reconcile this high column density with that inferred from the H_2 emission.

Figure 16 compares the observed and predicted (model from Fig. 15d) CO $v = 1-0$ spectrum, the latter made up of the contributions of both the hot and warm components. It should be noted that the apparent absorption of solid CO at 4.67 μm could be nothing more than the result of a fictitious continuum across the band that is the consequence of the limited spectral resolution. The calculations for the warm component include also ^{13}CO, with an adopted abundance 60 times lower than that of ^{12}CO. The contribution of the ^{13}CO $v = 1-0$ band can be identified in the modelled spectrum as a modulation of the continuum in the $P-$branch of CO, between 4.67 and 5 μm. A similar modulation can be observed in the SWS01 data, thus suggesting that weak ^{13}CO emission is also present in the observed spectrum. However, the ^{13}CO lines cannot account for the observed P-R-asymmetry in ^{12}CO. In the model for Peak 2, the intensity of the hot component is a factor of 2 weaker than at Peak 1.

4.4.3. Models for H_2O

The Einstein-A coefficients of the H_2O pure rotational transitions are much larger than those of CO. This implies that, for the densities of interest, the H_2O rotational

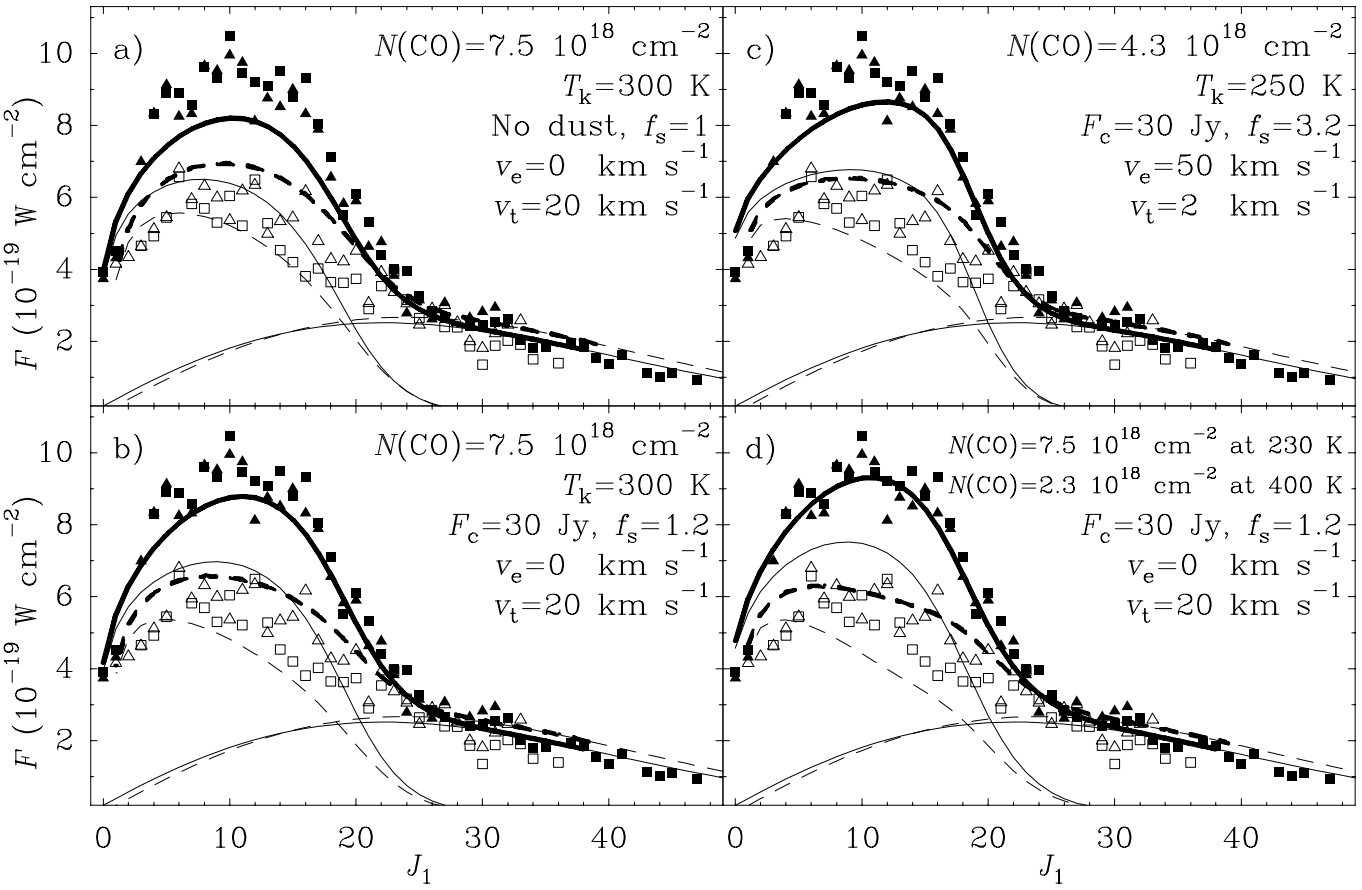

Fig. 15. CO $v = 1{-}0$ fluxes toward Peak 1 in the $P-$ (filled symbols) and $R-$ (open symbols) branches compared with model predictions. Triangles and squares indicate SWS06 and SWS01 data, respectively. Solid and dashed lines show results for the $P-$ and $R-$branch, respectively. Thin lines show predictions for the hot (3×10^3 K with $v = 0$ level populations in LTE) and warm (see text for details) components, and thick lines show the sum of both. Beam averaged CO column density, kinetic temperature, continuum flux, f_s factor, expansion velocity (v_e), and microturbulent velocity (v_t) used for the warm component are indicated in the corresponding panels.

levels of the ground vibrational state will not be populated according to LTE, and therefore the excitation conditions will be strikingly dependent on T_k, $n(H_2)$ and the H_2O column density (through radiative trapping). In the models below we assume $T_k = 300$ K (i.e., the average temperature inferred from the CO warm emission), and vary $n(H_2)$ and $N(H_2O)$ to fit the observed H_2O $\nu_2 = 1{-}0$ line fluxes.

First of all, it is easy to show that the relative fluxes of the $P-$ and $R-$branches (Figs. 5 and 17a) cannot be explained if the ro-vibrational lines are optically thin. In that case, relatively strong emission in the $1_{10} \rightarrow 1_{01}$ line at 6.18 μm and in the $2_{12} \rightarrow 1_{01}$ and $3_{03} \rightarrow 2_{12}$ lines at 6.05 μm is expected if the strongest $P-$branch lines are approximately matched. For $N(H_2O) \approx 10^{17}$ cm^{-2} (Fig. 17b), a few low-lying lines have peak opacities larger than 1 but still the above lines and the $1_{01} \rightarrow 1_{10}$ one are seriously overestimated. Neither the inclusion of dust, nor plausible variations in T_k and $n(H_2)$ solve this discrepancy. As shown in Fig. 17c, both the increase of $N(H_2O)$ and the effect of dust reduce the flux of the $R-$branch lines to an acceptable level (noise level). Also with $N(H_2O) \approx 10^{18}$ cm^{-2} and $n(H_2) \approx 2 \times 10^7$ cm^{-3}, most high-lying lines are approximately matched; this high $n(H_2)$ is consistent with the required thermalization of the pure rotational $v = 0$ CO lines discussed in Sect. 4.2.4.

The main drawback of the model from Fig. 17c is that the 6.86 μm spectral feature (composed of the $2_{21} \rightarrow 3_{30}$ and $2_{20} \rightarrow 3_{31}$) is expected to be the strongest one, whereas the observations indicate that the 6.5 and the 6.64 μm features are stronger (however, the latter may be contaminated by the [Ni II] line –RBD). It is worth noting that the 6.86 μm feature is actually the strongest toward BN (González-Alfonso et al. 1998). Also the model of Fig. 17c underestimates the flux of the $1_{11} \rightarrow 2_{20}$ line flux at 6.67 μm. Figure 18 displays the dependence of the 6.86-to-6.5 μm and of the 6.86-to-6.64 μm flux density ratios on $N(H_2O)$. For $n(H_2) = 5 \times 10^6$ cm^{-3} and $T_k = 300$ K, $N(H_2O)$ around 10^{17} cm^{-2} would match the observed flux density ratios of those features but, as pointed out above, the lack of emission in the $R-$branch would then remain unexplained. However, Fig. 18 also shows that the above flux ratios strongly depend on $n(H_2)$ and T_k. If the rotational excitation temperatures decrease, lower values

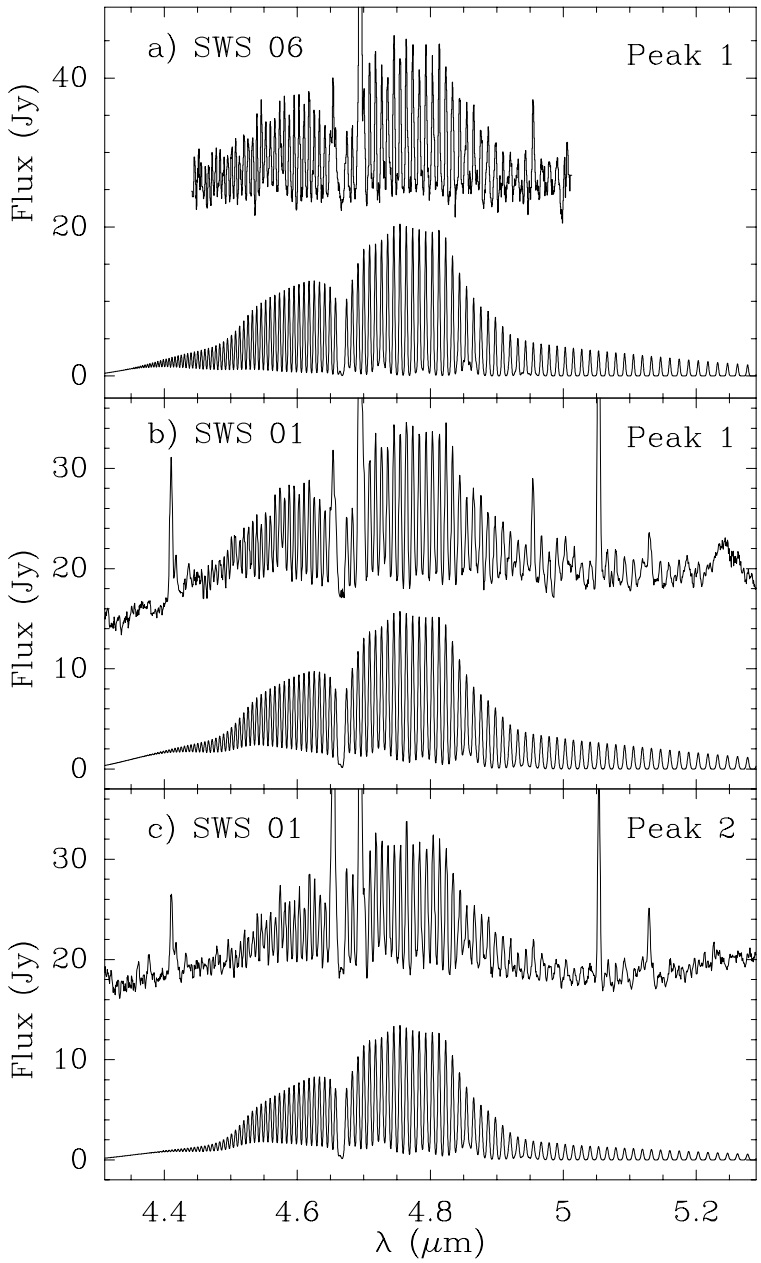

Fig. 16. Comparison between the observed CO $v = 1-0$ band and the composite hot-warm model prediction of Fig. 15d (after subtracting the continuum). An LTE $T_k = 3 \times 10^3$ K component has been assumed for the hot component, whereas the warm component includes ^{13}CO with an abundance 60 times lower than that of ^{12}CO. We have assumed $\lambda/\Delta\lambda = \lambda/\Delta\lambda(4.7\ \mu m) + 330(\lambda(\mu m) - 4.7)$, where $\lambda/\Delta\lambda(4.7\ \mu m) = 1150$ and 1500 in the SWS06 (panel **a)**) and SWS01 (panels **b)** and **c)**), respectively. The model for the warm component at Peak 2 only differs from that of Fig. 15d in the fact that the illuminating flux has been reduced by 10%. The observed SWS06 spectrum of Peak 1 and SWS 01 spectrum of Peak 2 have been shifted up 7 Jy and 8 Jy, respectively.

for the above ratios are expected at any $N(H_2O)$. Since these low-excitation conditions cannot reproduce the flux of other higher excitation lines, a gradient of physical conditions seems necessary to fit the H_2O band.

Figure 17d shows that a low excitation component (i.e., $T_k = 100$ K and $n(H_2) = 10^5$ cm^{-3}) favours just the fluxes of the $P-$lines which are underestimated in Fig. 17c. Thus the composite model of Fig. 17e, where the fluxes are the addition of those of Figs. 17c and 17d, reproduces reasonably the observed band shape. The conditions for the warm component ($T_k = 300$ K, $n(H_2) = 2\times10^7$ cm^{-3}) are consistent with those derived for CO.

Inspection of Fig. 19 may help to compare in more detail the model results of Fig. 17e and the observations. In Fig. 19a the "observed" and modeled column densities are both computed in the optically thin limit from Eq. (2). Figure 19b compares directly the predicted and observed line fluxes, the region between the

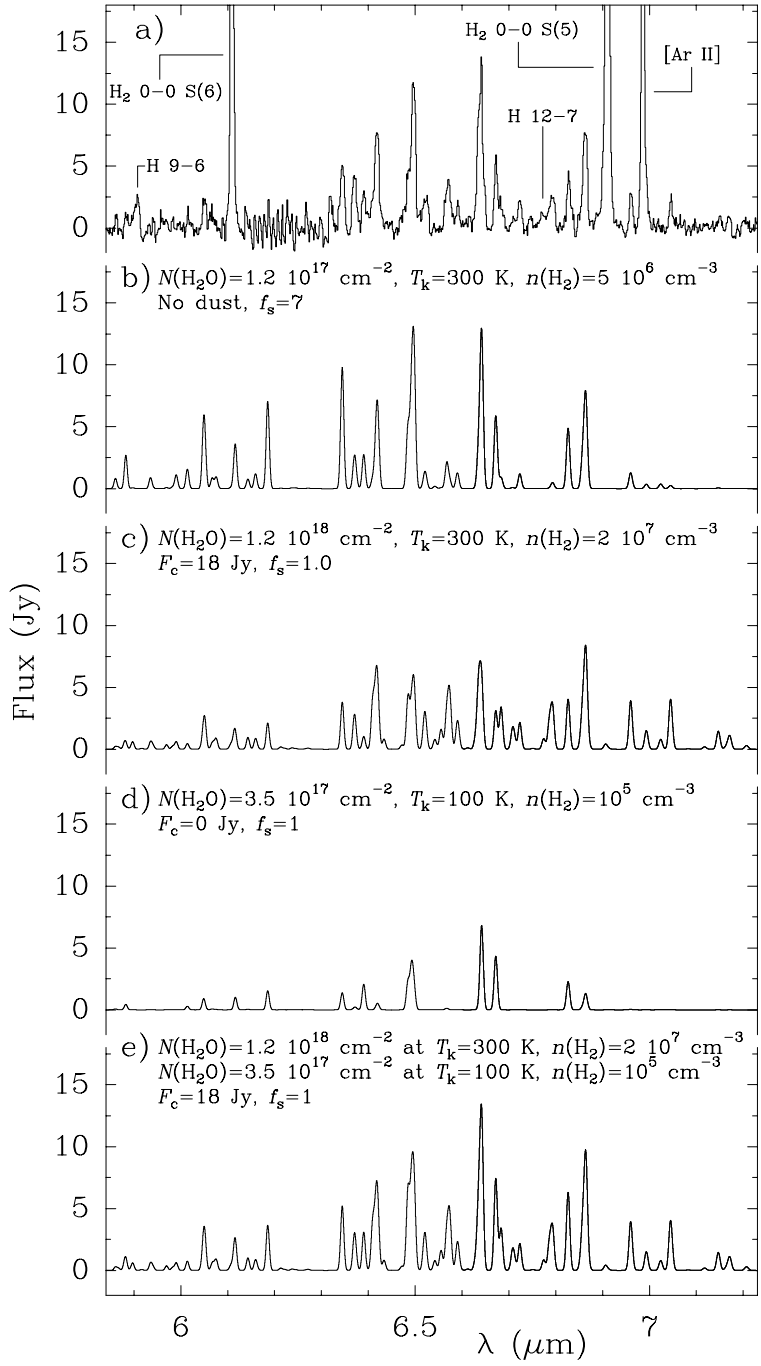

Fig. 17. Observed H_2O $\nu_2 = 1{-}0$ band toward Peak 1 **a)** and model predictions **b–e)**. In all the models $f_b = 0.7$, $v_t = 20\,km\,s^{-1}$, and $v_e = 0\,km\,s^{-1}$; other varying parameters are indicated in the corresponding panels. In **e)** the source is composed of the warm component in panel **c)** (300 K) and the colder (100 K) component in panel **d)**.

dashed lines indicating line fluxes which are reproduced within 50%. Only a few – labelled – lines lie out from that region. Most of them are lines that merge with others ($3_{13}\rightarrow2_{12}$, $2_{12}\rightarrow1_{01}$, $5_{05}\rightarrow6_{16}$, $2_{02}\rightarrow2_{11}$, $3_{30}\rightarrow4_{41}$, $0_{00}\rightarrow1_{11}$, $1_{01}\rightarrow2_{12}$, $3_{03}\rightarrow4_{14}$), are weak lines of the $R-$branch ($2_{21}\rightarrow2_{12}$, $2_{21}\rightarrow1_{10}$, $2_{20}\rightarrow1_{11}$), or lie in a spectral region of relatively high noise ($1_{10}\rightarrow1_{01}$), so that the measured fluxes are uncertain. The main discrepancy concerns the $5_{23}\rightarrow5_{32}$ line (E_u = 2950 K), the flux of which is underestimated by a factor of ≈3.5. At Peak 1, this line appears as a wing of the strong 6.5 μm spectral feature, but it is more clearly detected toward Peak 2 (Fig. 5b). With T_k and $N(H_2O)$ from Fig. 17c, an H_2 density of $\approx10^8$ cm^{-3} is required to match its line flux. However, other high-lying lines such as the $4_{23}\rightarrow4_{32}$ at 6.556 μm (E_u = 2750 K) are overestimated in the model of Fig. 17c, and therefore these discrepancies do not seem significant in view of the uncertainties regarding the collisional rates for pure rotational transitions. In the model of Fig. 17c, lines with $E_u > 2650$ K are

optically thin, whereas most lines with $E_u < 2550$ K are optically thick but with moderate opacities (<10). The source-averaged $N(H_2O)$ of 1.2×10^{18} cm^{-2} corresponds to a radial $N(H_2O)$ of 2.1×10^{17} cm^{-2}, which is in agreement within a factor of 2 with the value we inferred toward BN (González-Alfonso et al. 1998). The values of $n(H_2)$ and T_k derived here are higher than in the model for BN, because the shell is located much further from the star and therefore the stellar radiation has a negligible influence on the distribution of populations in the ground vibrational state.

We have also performed some models for H_2O at $T_k = 3 \times 10^3$ K to estimate the possible contribution to the H_2O band from the hot component. Since radiative trapping in the hot component is not important, excitation temperatures in the ground vibrational state will be moderate despite the high T_k, and then significant line emission will arise just in the same lines that account for the emission from the warm component. Therefore, we can only give upper limits for $N(H_2O)$ that do not conflict with the observed line fluxes. Assuming that the CO emission is pumped through collisions with H_2, i.e., $n(H_2) = 3 \times 10^8$ cm^{-3} and $n(H) = 0$ (Sect. 4.2.5), $N(H_2O)$ above 2.5×10^{15} cm^{-2} would imply some line fluxes larger than observed (for $N(H_2O) = 2.5 \times 10^{15}$ cm^{-2}, the $1_{01} \rightarrow 1_{10}$ line is expected to arise entirely from this hot component, but the $5_{23} \rightarrow 5_{32}$ line is still underestimated). On the other hand, if collisions with atomic hydrogen are responsible for the CO emission from the hot component, i.e., $n(H) = n(H_2) = 10^7$ cm^{-3}, the upper limit found for $N(H_2O)$ is $\sim 3 \times 10^{16}$ cm^{-2}. In this case, significant emission is predicted to arise only from low-lying lines, and the relatively high upper limit found for $N(H_2O)$ is a consequence of the fact that T-V energy transfer in H_2O-H collisions is only slightly enhanced relative to H_2O-H_2 collisions (Fig. 9). In conclusion, we estimate that H_2O is less abundant than CO in the hot component if CO $v = 1$ is excited through collisions with H_2, but the relative abundances will be much more uncertain if the density of atomic H is high (this conclusion, however, is subject to the uncertainties regarding the collisional rates for H_2O-H excitation).

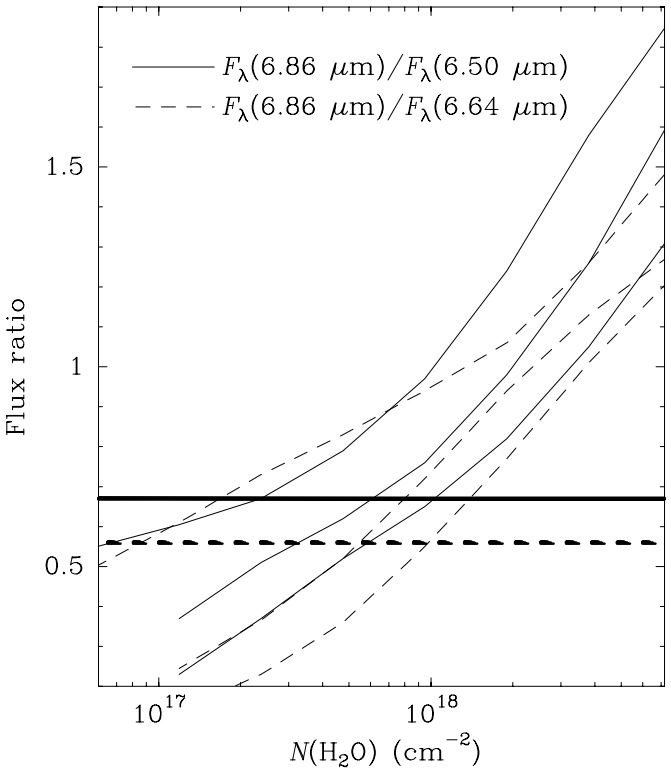

Fig. 18. Predicted flux ratio relation for the 6.86 μm to 6.5 μm spectral features (solid lines), and for the 6.86 μm to the 6.64 μm spectral features (dashed lines), versus beam-averaged H_2O column density. The 6.86 μm feature corresponds to the joint emission of the H_2O $\nu_2 = 1$–0 $2_{21} \rightarrow 3_{30}$ and the $2_{20} \rightarrow 3_{31}$ lines, the 6.5 μm feature is the joint emission of the H_2O $\nu_2 = 1$–0 $1_{01} \rightarrow 2_{12}$ and the $2_{12} \rightarrow 3_{03}$ lines, and the 6.64 μm feature is the joint emission of the H_2O $\nu_2 = 1$–0 $1_{10} \rightarrow 2_{21}$ and the $3_{03} \rightarrow 4_{14}$ lines. Upper lines: $n(H_2) = 5 \times 10^6$ cm^{-3}, $T_k = 300$ K; middle lines: $n(H_2) = 5 \times 10^5$ cm^{-3}, $T_k = 150$ K; lower lines: $n(H_2) = 2.5 \times 10^5$ cm^{-3}, $T_k = 100$ K. For all the calculations $f_s = 1$, $f_b = 0.7$, $v_t = 20$ km s^{-1}, $v_e = 0$ km s^{-1}, and dust is not included. Horizontal thick lines indicate the observed values at Peak 1. Toward Peak 2, the observed values are 0.74 (solid line) and 0.71 (dashed line).

5. Discussion and conclusions

5.1. The CO/H_2O abundance ratio

In our best-fit models for the warm component, the source-averaged column densities for CO and H_2O in Peak 1 and Peak 2 are $5-10 \times 10^{18}$ cm^{-2} and $1-2 \times 10^{18}$ cm^{-2}, respectively (Sects. 4.2.3, 4.2.4, 4.4.2, and 4.4.3). Although these values are subject to considerable uncertainty, the abundance ratio is more reliable. From the discussion in Sect. 4.2.3, we conclude that CO is more abundant, by at least a factor of 2, than H_2O in the SWS beam around Peak 1 and 2. Concerning the hot component in Peak 1, it seems that CO is also more abundant than H_2O (Sect. 4.4.3), but this result strongly depends on the assumed H_2 dissociation fraction.

Unfortunately, abundances relative to H_2 are more difficult to infer because, although the ISO/SWS beam for the CO and H_2O bands is the same as the beam for most of the H_2 lines, in the warm component (*i*) the H_2 lines are optically thin but the CO and H_2O lines are optically thick; (*ii*) H_2 is excited through collisions (RBD) but the CO $v = 1$ and the H_2O $\nu_2 = 1$ vibrational states are radiatively pumped; (*iii*) only a few lowest-lying H_2 lines trace regions with $T_k \leq 400$ K, where the warm CO and H_2O emissions arise, and the kinetic temperature inferred from those H_2 lines is not well constrained (as a consequence, in part, of the uncertainty in the flux of the H_2 0–0 S(0) line). Nevertheless, in Sect. 4.2.4 we have argued that the beam-averaged $N(H_2)$ above 200 K at both peaks imposes an upper limit on the beam-averaged $N(CO)$ of $\approx 3.5 \times 10^{18}$ cm^{-2}, and therefore a beam filling

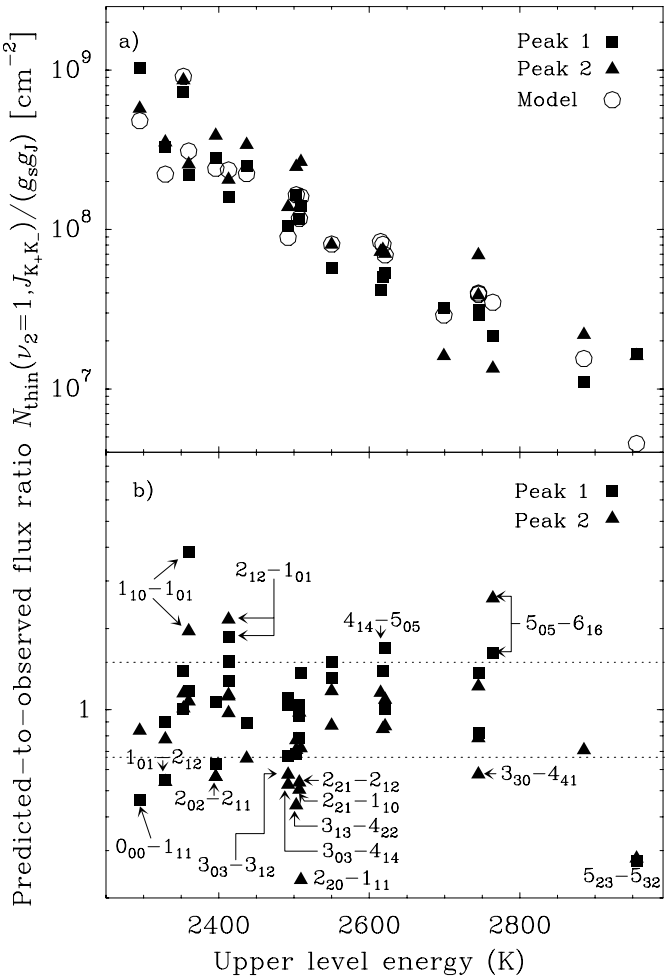

Fig. 19. a) H_2O upper level column densities toward Orion/Peak 1 (squares) and Peak 2 (triangles), compared with the model prediction of Fig. 17e (circles). Column densities have been calculated from Eq. (2) (i.e., as proportional to the line fluxes) and by using the same lines for the observations and the model. **b)** Predicted-to-observed flux ratios. Dotted lines indicate values of 0.66 and 1.5.

factor of 2–3 and a possible substantial fraction of atomic hydrogen are invoked to reconcile this upper limit with the larger source-averaged N(CO) required to match the observed P-R-asymmetry. In the hot component, and even assuming that the high-J CO emission arises in the same region as the high excitation lines of H_2 (RBD), the CO to H_2 abundance ratio will strongly depend on the assumed dissociation fraction and density.

The CO/H_2O abundance ratio derived at both peaks does not match the predictions for C-shock models. Once the temperature across a C-shock exceeds 400 K, most oxygen not bound in CO molecules is expected to form H_2O molecules for a wide range of preshock densities and shock velocities larger than 15 km s^{-1} (Kaufman & Neufeld 1996a, 1996b). Adopting the gas-phase abundances for oxygen and carbon nuclei of 3.2×10^{-4} (Meyer et al. 1994; Meyer et al. 1998) and 1.4×10^{-4} (Cardelli et al. 1996; Sofia et al. 1997) relative to H nuclei, respectively, and assuming that all carbon is bound in CO molecules, the expected H_2O abundance is a factor 1.3 higher than the CO abundance, and will increase above this value if grain mantles return efficiently to the gas phase at the shock. This is contrary to the inferred CO/H_2O relative abundances.

5.2. The hot component

The CO band emission in Peak 1 reveals a component with high temperature ($T_k \sim 3 \times 10^3$ K), high density ($>10^7$ cm^{-3}), and an uncertain but probably high dissociation fraction (Sect. 4.2.3). In principle, the required CO excitation could be ascribed to collisions with H_2 alone by invoking H_2 densities large enough ($\geq 3 \times 10^8$ cm^{-3}). However, the combination of these high values of $n(H_2)$ and T_k leads to interpretation problems when one attempts to identify the emitting region with the hottest part of a C-shock. In C-shocks, the compression factor in the hottest region is relatively low, so that the high density required to produce the observed CO emission requires high preshock densities, as in the models of Kaufman & Neufeld (1996b). In these models, however, the maximum temperature of the neutral component hardly approaches the required T_k of 3×10^3 K without reaching the breakdown conditions that lead to a jump shock (Fig. 4 of Kaufman & Neufeld 1996b).

It seems therefore necessary to invoke collisions with atomic hydrogen, but again C-type shocks hardly account for the required dissociation fraction. Models of C-shocks specifically applied to the Orion/Peak 1 shock yield dissociation fractions less than 10% (Draine & Roberge 1982; Chernoff et al. 1982). Henceforth high preshock densities are again required but, apart from the above temperature problem, the dissociation fraction is expected to remain very low (less than 1% in the models of Kaufman & Neufeld 1996b).

HM predict for a J-shock high H I densities at temperatures larger than 400–500 K, where H_2 has not been reformed yet on dust grains. CO is not easily destroyed at the shock front because of its high binding energy, but may be chemically dissociated downstream at $T_k > 3 \times 10^3$ K by endothermic reaction with H I, and photodissociated by the FUV field. Nevertheless, once CO has self-shielded all carbon can be channelled into CO even when the H_2 abundance is low (HM). Similar theoretical results have been found by Neufeld & Dalgarno (1989). Since the CO abundance is larger than 10^{-5} at $T_k < 10^4$ K (at least in the HM standard model), and the compression factor is typically 10^2 (Hollenbach & McKee 1979), a J-shock appears as a promising way to explain the emission from the hot component. Furthermore, the lack of large amounts of H_2O at this temperature is readily explained by the fact that H_2O formation follows that of H_2. On the other hand, Smith (1991) suggested that, in fast bow shocks, high H densities would coexist with CO at $T_k \sim 3 \times 10^3$ K in the transition zone between the leading dissociative

Table 1. Physical parameters derived for Peak 1 and Peak 2.

Component	T_k (K)	$n(H_2)^a$ (cm^{-3})	$N(CO)^b$ (cm^{-2})	$N(H_2O)^b$ (cm^{-2})	Excitation	Shock type[c]
Warm	200–400	$\sim 2\times10^7$	$5-10\times10^{18}$	$1-2\times10^{18}$	Radiative	C
Hot	$\sim 3\times10^3$	$\geq 10^7$	$\sim 10^{16}$	$<3\times10^{16}$	Collisional	J

[a] For the hot component, lower limit required to match the CO band shape for $T_k = 3\times10^3$ K.
[b] Source-averaged column densities (in the warm component, beam-averaged values will be lower according to the beam-filling factor). For the hot component, (*i*) we have assumed $n(H) = 10^7$ cm^{-3}, and (*ii*) at Peak 2 $N(CO)$ will be half of the quoted value.
[c] Type of shock that better matches the properties of the emission. Some contribution of a J-shock to the warm component may be present.

J-shock and the C-shock at the bow flanks. This interpretation is consistent with the NICMOS image of the Orion BN/KL region (Stolovy et al. 1998), where clumps shaped as bow shocks are observed in the emission of H_2 $v = 1-0$ $S(1)$. The high H I density required to explain the observed CO emission gives additional support to the suspicion of RBD that H_2 formation pumping could account for some of the emission in the high-lying H_2 lines. The total CO emission from the hot component toward Peak 1, including both the pure rotational and the rovibrational lines, is $\sim$0.1 erg s^{-1} cm^{-2} sr^{-1}. This value is comparable with the total H_2 emission in the same aperture (0.28 erg s^{-1} cm^{-2} sr^{-1}, RBD), and indicates that CO is an important coolant of the hot gas.

It is worth noting that the CO emission from the hot component, which is at Peak 1 a factor of $\sim$2 stronger than at Peak 2, is – unlike the warm component – roughly correlated with the H_2 emission: the H_2 column density at Peak 1 is a factor $\approx$1.5 higher than at Peak 2 (Wright 2000). (For some individual H_2 lines whose upper energy level is above 10^4 K, as the 0–0 S(9), the Peak 1-to-Peak 2 intensity ratio is closer to 2.) In combination with the facts that the CO hot emission is optically thin, it is excited through collisions, and traces a region of high temperature (i.e., properties similar to those of the H_2 emission), this strongly suggests that the bulk of the H_2 emission and the CO emission from the hot component arise in the same region. The observed CO emission will impose important constraints on any model that attempts to explain the emission from the H_2 high energy levels.

5.3. The warm component

At both peaks, the emission from the warm component is found to arise from resonant scattering (Sect. 4.2.2). Both the CO and H_2O band shapes and the observed P-R-asymmetry indicate a moderate temperature (200–400 K) and high column density. Our derived radial $N(CO)$ ($1-2\times10^{18}$ cm^{-2}) is not far from the value of 3.5×10^{18} cm^{-2} predicted by Draine & Roberge (1982) for the Orion/Peak 1 C-shock model. It is unclear, however, if the band shape can be matched by this shock model, once scattering and opacity effects are taken into account. If so, moderate values of the shock speed should be involved (Fig. 14 of Draine & Roberge 1984), and this would also account for the relative weakness of the H_2 1–0 $S(1)$ line at the position where the CO $P(8)$ line is strongest (GG). The underabundance of H_2O relative to CO could be the result of H_2O photodissociation by the FUV radiation field in OMC-1.

Some contribution from a J-shock cannot, however, be disregarded. J-shock models predict a dominant temperature component at $T_k \sim 400$ K, which is the result of the heating of gas through collisional de-excitation of newly formed H_2 in the molecular reformation region (HM; Elitzur et al. 1989; Neufeld & Dalgarno 1989). The temperature of the "plateau" coincides rather well with the upper limit found for the CO emission in the warm component. HM predict for this plateau $N(CO) \sim 10^{18}$ b cm^{-2}, where $b = v_A/1.84$ and v_A is the Alfvén velocity in km s^{-1}, similar to our derived radial $N(CO)$ for $b = 1-2$. The main discrepancy concerns the low H_2O abundance generally predicted by J-shock models. The predicted $N(H_2O)$ is a factor >25 lower than $N(CO)$ for shock speeds faster than 60 km s^{-1} and preshock densities $n_0 \leq 10^6$ cm^{-3} (Neufeld & Dalgarno 1989). Preshock densities larger than *a few* $\times 10^6$ cm^{-3} would be needed to explain the inferred $N(H_2O)$, but it seems unlikely that these conditions apply to the whole region covered by the ISO/SWS beam. Anyway, some contribution of a J-shock to the observed CO emission may also explain the underabundance of H_2O relative to CO. This possibility is strengthened from the fact that the H_2O-to-CO flux ratio is larger at Peak 2 than at Peak 1, whereas the CO emission from the hot component is weaker toward Peak 2.

Since the observed warm rovibrational emission arises from resonant scattering, it does not contribute to the cooling of the postshock gas; in fact, the conversion of $R-$branch photons into $P-$branch photons involves some heating of the gas through thermalization of the energy excess. The unobserved pure rotational emission will be responsible for the cooling. Despite the underabundance of H_2O, it still dominates the cooling because of its high dipolar moment. From our models we estimate that the total warm rotational emission in the direction of Peak 1 is $\sim$0.2 and $\sim$1 erg s^{-1} cm^{-2} sr^{-1} for CO and H_2O,

respectively. The uncertainties are considerable (a factor of 3) but still the cooling contribution by H_2O is expected to be larger than by H_2 (total emission of 0.28 erg s^{-1} cm^{-2} sr^{-1} toward Peak 1, RBD). This is predicted for *C*-shock models with high preshock densities (Kaufman & Neufeld 1996b).

5.4. Peak 1/Peak 2

The CO emission (flux and band shape) from the warm component (i.e., once the emission from the hot component has been subtracted) is very similar toward Peak 1 and Peak 2, whereas the H_2O emission is slightly stronger toward Peak 2 (Sect. 3.1.1). In principle, this is unexpected in view of the relative intensities of the H_2 lines at both positions. This lack of correlation can be attributed to the fact that CO and H_2O trace regions colder than those traced by most H_2 lines. Other possible causes are (*i*) CO/H_2O and H_2 are excited through different mechanisms, and are therefore sensitive to different physical parameters (flux of radiation against density); (*ii*) the CO/H_2O lines are optically thick and the H_2 lines are optically thin, and therefore the sensitivity of their emission to variations of column density is different; and (*iii*) the bulk of the H_2 emission and that of the CO and H_2O could originate in different flows, as the spatial shift between the CO $P(8)$ line and Peak 1 (GG) suggests.

Some differences are still found in the CO and H_2O spectra toward both peaks, which suggest that the column density of the warm gas, and perhaps also the density, are larger toward Peak 2. These are (*i*) the relative enhancement of the CO low-J lines toward Peak 2; (*ii*) some high-lying H_2O P–lines are a factor of ≈2 stronger at this position; and (*iii*) the modulation of the continuum in the $P-$branch of the CO band, attributable to the contribution of ^{13}CO (Fig. 16), is more striking at Peak 2 than at Peak 1 (Figs. 1 and 16). However, differences in column density and density between both peaks are not expected to be larger than a factor of 2, and since the uncertainties in the physical conditions inferred from our models are larger, we have not attempted to model the emission from both peaks separately.

6. Summary

We have analyzed the CO $v = 1-0$ and H_2O $\nu_2 = 1-0$ molecular bands in the the ISO/SWS spectra of Orion Peak 1 and Peak 2. Our main results are:

1. The CO band reveals the presence of two components: a warm component, with kinetic temperature of 200–400 K, and a hot component, with T_k around 3×10^3 K. The $P-$branch emission from the warm component is a factor ∼2 stronger than the $R-$branch.

2. The H_2O emission arises from a region with characteristics similar to those of the CO warm component. The $P-$branch emission is also much stronger than the $R-$branch, which is hardly detected.

3. Neither the warm CO or H_2O emission can be explained in terms of collisional excitation. Resonant scattering of photons coming from the strongest infrared sources in Orion BN/KL is invoked to account for it.

4. The CO band shape, band flux, and P-R-asymmetry indicate large source-averaged CO column densities ($5-10\times 10^{18}$ cm^{-2}) that can be hardly reconciled with the observed -too weak- emission from the low-J H_2 lines. Beam-filling in the optically thick CO emission and/or a substantial H_2 dissociation fraction are invoked to solve this discrepancy.

5. The density inferred from the H_2O emission is $\sim 2 \times 10^7$ cm^{-3}. The P-R-asymmetry observed in H_2O also indicates optically thick emission, but the H_2O column density in the warm component is at least a factor of 2 lower than the column density of CO.

6. A C-type shock could in principle account for the CO and H_2O emissions from the warm component. The underabundance of H_2O relative to CO could be the consequence of H_2O photodissociation, or of the contribution from a jump shock to the CO emission.

7. The warm CO and H_2O column densities are probably somewhat larger toward Peak 2 than toward Peak 1.

8. The emission from the hot component is only clearly detected in CO. The flux is a factor of ≈2 larger at Peak 1 than at Peak 2. CO excitation is pumped through collisions, and the hot CO emission seems to arise in the same region where the bulk of the H_2 emission is generated.

9. In order to explain the CO emission from the hot component through collisions with H_2, a high H_2 density ($\sim 3 \times 10^8$ cm^{-3}) is required to reconcile the hot H_2 and CO column densities. However, collisions with atomic hydrogen in a dissociative shock may better account for this component.

Acknowledgements. We thank A. Rodríguez-Franco for providing us with the spectra of the CO $J = 1-0$ and $2-1$ millimetric lines toward Orion BN/KL. This work has been partially supported by the Spanish DGICYT under grant PB90-408 and by UAH under grant UAH2002/079. CMW acknowledges support from an ARC Australian Postdoctoral Fellowship.

References

Ayres, T. R., & Wiedemann, G. R. 1989, ApJ, 338, 1033
Beckwith, S., Persson, S. E., Neugebauer, G., & Becklin, E. E. 1978, ApJ, 223, 464
Bieniek, R. J., & Green, S. 1983, ApJ, 265, L29
Cardelli, J. A., Meyer, D. M., Jura, M., & Savage, B. D. 1996, ApJ, 467, 334
Cernicharo, J., González-Alfonso, E., Alcolea, J., Bachiller, R., & John, D. 1994, ApJ, 432, L59
Cernicharo, J., Pardo, J. R., González-Alfonso, E., et al. 1999a, ApJ, 520, L131
Cernicharo, J., González-Alfonso, E., Sempere, M. J., et al. 1999b, in ESA-SP Conf. The Universe as Seen by ISO, ed. P. Cox, & M. F. Kessler, 427

Chawla, G. K., McBane, G. C., Houston, P. L., & Schatz, G. C. 1988, J. Chem. Phys., 88, 5481
Chernoff, D. F., Hollenbach, D. J., & McKee, C. F. 1982, ApJ, 259, L97
DePristo, A. E., Augustin, S. D., Ramaswamy, R., & Rabitz, H. 1979, J. Chem. Phys., 71, 850
de Graauw, Th., Haser, L., Beintema, D. 1996, A&A, 315, L49
Draine, B. T. 1980, ApJ, 241, 1021
Draine, B. T., & Roberge, W. G. 1982, ApJ, 259, L91
Draine, B. T., & Roberge, W. G. 1984, ApJ, 282, 491
Draine, B. T., Roberge, W. G., & Dalgarno, A. 1983, ApJ, 264, 485
Elitzur, M. 1980, ApJ, 240, 553
Elitzur, M., Hollenbach, D. J., & McKee, C. F. 1989, ApJ, 346, 983
Evans II, N. J., Lacy, J. H., & Carr, J. S. 1991, ApJ, 383, 674
Geballe, T. R., & Garden, R. P. 1987, ApJ, 317, L107
Geballe, T. R., & Garden, R. P. 1990, ApJ, 365, 602 (GG)
Geballe, T. R. 1993, in Astronomical Infrared Spectroscopy: Future Observational Directions, ed. S. Kwok, ASP Conf. Ser., 41, 147
Genzel, R., Reid, M. J., Moran, J. M., & Downes, D. 1981, ApJ, 244, 884
Gezari, D. Y., Backman, D. E., & Werner, M. W. 1998, ApJ, 509, 283
Glass, G. P., & Kironde, S. 1982, J. Phys. Chem., 86, 908
González-Alfonso, E., & Cernicharo, J. 1997, A&A, 322, 938
González-Alfonso, E., & Cernicharo, J. 1999, ApJ, 525, 845
González-Alfonso, E., Cernicharo, J., van Dishoeck, E. F., Wright, C. M., & Heras, A. 1998, ApJ, 502, L169
Grasdalen, G. L., Hackwell, J. A., Lynch, D. K., & Russell, R. W. 1992, ApJ, 397, L119
Green, S., & Thaddeus, P. 1976, ApJ, 205, 766
Green, S., Maluendes, S., & McLean, A. D. 1993, ApJS, 85, 181
Green, S., Keller, H. M., Schinke, R., & Werner, H. J. 1996, J. Chem. Phys., 105, 5416
Harwit, M., Neufeld, D. A., Melnick, G. J., & Kaufman, M. J. 1998, ApJ, 497, L105
Hasegawa, T., & Akabane, K. 1984, ApJ, 287, L91
Hollenbach, D. J., & McKee, C. F. 1979, ApJS, 41, 555
Hollenbach, D. J., & McKee, C. F. 1989, ApJ, 342, 306 (HM)
Hooker, W. J., & Millikan, R. C. 1962, J. Chem. Phys., 38, 214
Jaffe, D. T., & Martín-Pintado, J. 1999, ApJ, 520, 162
Kaufman, M. J., & Neufeld, D. A. 1996a, ApJ, 456, 611
Kaufman, M. J., & Neufeld, D. A. 1996b, ApJ, 456, 250
Kim, Y. H., & Micha, D. A. 1989, J. Chem. Phys., 90, 5486
Lee, H. M., & Draine, B. T. 1985, ApJ, 290, 211
Lee, K. T., & Bowman, J. M. 1987, J. Chem. Phys., 86, 215
Leech, K., de Graauw, T., van den Ancker, M., et al. 2001, ISO Handbook, vol. VI (SWS) SAI/2000-008/Dc, `http://www.iso.vilspa.esa.es/manuals/HANDBOOK/VI/sws_hb`
Lutz, D., Feuchtgruber, H., & Morfill, J. 2000, ISO-SWS grating resolution and instrumental profile as measured by the full resolution modes SWS02 and SWS06, ISO-99-1 V1.0
McBane, G. C., Kable, S. H., Houston, P. L., & Schatz, G. C. 1991, J. Chem. Phys., 94, 1141
Melnick, G. J., Ashby, M. L. N., Plume, R., et al. 2000, ApJ, 539, L87
Meyer, D. M., Jura, M., Hawkins, I., & Cardelli, J. A. 1994, ApJ, 437, L59
Meyer, D. M., Jura, M., & Cardelli, J. A. 1998, ApJ, 493, 222
Miller, D. J., & Millikan, R. C. 1970, J. Chem. Phys., 53, 3384
Millikan, R. C., & White, D. R. 1963, J. Chem. Phys., 39, 3209
Neufeld, D. A., & Dalgarno, A. 1989, ApJ, 340, 869
O'Brien, I., & Drury, L.O'C. 1996, MNRAS, 280, 550
Parker, G. A., & Pack, R. T. 1978, J. Chem. Phys., 68, 1585
Reid, J. P., Simpson, C. J. S. M., & Quiney, H. M. 1997, J. Chem. Phys., 106, 4931
Rodríguez-Franco, A., Martín-Pintado, J., & Wilson, T. L. 1999, A&A, 344, L57
Rosenthal, D., Bertoldi, F., & Drapatz, S. 2000, A&A, 356, 705 (RBD)
Sahai, R., & Wannier, P. G. 1985, ApJ, 299, 424
Schinke, R., Engel, V., Buck, U., Meyer, H., & Diercksen, G. H. F. 1985, ApJ, 299, 939
Scoville, N., Kleinmann, S. G., Hall, D. N. B., & Ridgway, S. T. 1983, ApJ, 275, 201
Sempere, M. J., Cernicharo, J., Lefloch, B., González-Alfonso, E., & Leeks, S. 2000, ApJ, 530, L123
Smith, M. D. 1991, MNRAS, 253, 175
Snell, R. L., Howe, J. E., Ashby, M. L. N., et al. 2000, ApJ, 539, L93
Sofia, U. J., Cardelli, J. A., Guerin, K. P., & Meyer, D. M. 1997, ApJ, 482, L105
Stolovy, S. R., Burton, M. G., Erickson, E., et al. 1998, ApJ, 492, L151
Storey, J. W. V., Watson, D. M., Townes, C. H., Haller, E. E., & Hansen, W. L. 1981, ApJ, 247, 136
Thompson, R. I. 1973, ApJ, 181, 1039
van Dishoeck, E. F., Wright, C. M., Cernicharo, J., et al. 1998, ApJ, 502, L173
Vannier, L., Lemaire, J. L., Field, D., et al. 2001, A&A, 366, 651
von Rosenberg, C. W., Taylor, R. L., & Teare, J. D. 1971, J. Chem. Phys., 54, 1974
Watson, W. D., Elitzur, M., & Bieniek, R. J. 1980, ApJ, 240, 547
Watson, D. M., Genzel, R., Townes, C. H., & Storey, J. W. V. 1985, ApJ, 298, 316
Wight, C. A., & Leone, S. R. 1983, J. Chem. Phys., 78, 4875
Wright, C. M. 2000, in Astrochemistry: From Molecular Clouds to Planetary Systems, ed. Y. C. Minh, & E. F. van Dishoeck, 177
Wright, C. M., van Dishoeck, E. F., Black, J. H., et al. 2000, A&A, 358, 689
Wright, M. C. H., Sandell, D. J., Wilner, D., & Plambeck, R. L. 1992, ApJ, 393, 225
Wynn-Williams, C. G., Genzel, R., Becklin, E. E., Downes, D. 1984, ApJ, 281, 172